PHILOSOPHICAL TRANSACTIONS OF THE ROYAL SOCIETY A
MATHEMATICAL, PHYSICAL & ENGINEERING SCIENCES

Motion of a Granular Avalanche in an Exponentially Curved Chute: Experiments and Theoretical Predictions

Kolumban Hutter and Thilo Koch

Phil. Trans. R. Soc. Lond. A 1991 **334**, 93-138
doi: 10.1098/rsta.1991.0004

Motion of a granular avalanche in an exponentially curved chute: experiments and theoretical predictions

By Kolumban Hutter and Thilo Koch
Department of Mechanics, Technological Institute, D-6100 Darmstadt, F.R.G.

Contents

This paper describes a model to predict the flow of an initially stationary mass of cohesionless granular material down a rough curved bed, and checks it against laboratory experiments that were conducted with several cohesionless granular

Phil. Trans. R. Soc. Lond. A (1991) **334**, 93–138
Printed in Great Britain

materials that are released from rest and travel in an exponentially curved chute. This work is of interest in connection with the motion of rock and ice avalanches and dense flow snow avalanches.

We use the depth-averaged field equations of balance of mass and linear momentum as presented by Savage & Hutter (1990). These equations are evolution equations for the transversely averaged streamwise velocity and the distribution of avalanche depths and involve two phenomenological parameters, the internal angle of friction, ϕ, and a bed friction angle, δ, both as constitutive properties of Coulomb-type behaviour. We present the model but do not derive its equations, which are presented in two variants that incorporate weak and strong curvature effects. For granular avalanches which start as parabolic piles, the governing equations (incorporating weak curvature effects) permit similarity solutions. These solutions preserve the parabolic shape and have simple velocity distributions. We present the equations again without detailed explanations.

Experiments were performed with seven different granular materials (two classes of glass beads, Vestolen plastic particles, two samples of quartz granules and two types of crunched marmor particles). Piles of finite masses of such granular materials with various initial geometries were released from rest in a 100 mm wide chute having an exponentially curved bed that was lined with Makrolon (a plexiglass), drawing-paper and sandpaper. The granular masses under motion were photographed and video filmed and thus the geometry of the avalanche was recorded as a function of position and time. With all materials and for all the bed linings, the angle of repose and the bed friction angle were determined. The former was identified with the static internal angle of friction. Using a second measuring technique, the effects of the chute walls on the bed friction angle was experimentally determined and incorporated in an effective bed friction angle which thus showed a linear dependence on the pile depth. Coefficients of restitution were also estimated for the particles on the different bed linings.

The numerical integration scheme for the general model that was proposed earlier by Savage & Hutter (1989) is a lagrangian finite difference scheme which incorporates numerical diffusion. We present this scheme and analyse its reliability when the numerical diffusion is varied. We also discuss the integration procedure for the similarity solutions.

Comparison of the theoretical results with experiments pertain to the similarity model (SM) and the general equation model (GM). Crucial in such comparisons is the identification of initial condition which is not unique from the observational data. For SM it is shown that no initial condition can be found, in general, that would yield computational predictions of the evolution of the position of the leading and trailing edges of the granular avalanche in sufficient agreement with observations. When depth-to-length ratios of the initial pile geometry and the curvature of the bed are sufficiently small, however, then the SM solutions may be used for diagnostic purposes.

We finally compare experimental results with computational findings of the GM equations for many combinations of masses of the granular materials and bed linings. It is found that experimental results and theoretical predictions agree satisfactorily if the internal angle of friction, ϕ, exceeds the total bed friction angle, δ, or is not close to it. Limited variations of the bed friction angle along the bed do not seem to have a sizeable effect on the computational results, but it is important that dynamic values rather than static values for ϕ and δ are used in the computations. When δ is

very close to ϕ and $\delta < \phi$, the computational travel time of the granular avalanche exceeds the travel time of experiments considerably. Furthermore, when avalanche masses are reasonably small and coefficients of restitution of the granules on the bed relatively high, again the predictions of the theory overestimate travel times and underestimate avalanche lengths. Thus the theory does seem to be reasonable when the bed friction angle is definitely smaller than the internal angle of friction.

1. Introduction

Owing to the increased air pollution of recent years and the related problems with the dying forest mountainous regions have experienced a greater potential for the occurrence of slow-moving landslides, as well as for more rapidly flowing rock, ice and snow avalanches. This is the likely reason why in the past few years new mathematical descriptions for the motion of rock slides, sturz stroms, ice and snow avalanches have been presented in an attempt to better predict flow behaviour and runout distances.

The original simple fluid or particle models of Voellmy (1955), Salm (1968) and Perla & Martinelli (1978) or Perla *et al.* (1980) that were employed for the dynamics of both dense flow and powder snow avalanches (by an adequate adjustment of a frictional coefficient) are now gradually being extended or superseded by theories that describe the respective physical situations in more detailed and complete ways. Gravity-driven rock and ice avalanches and dense flow avalanches (these are flow avalanches in which the snow does not become airborne) are distinct from powder snow avalanches and governed by particle to particle collisions that cause the granular mass to behave in a fluid like fashion. We refrain from mentioning the relevant literature concerning constitutive behaviour here, because Savage & Hutter (1989, 1990) have demonstrated that a much simpler 'hydraulic' model with a Coulomb-type basal friction law is likely to be sufficient to predict the main features of these flows. Such a model is analogous to that used in hydraulics in which the dynamics is simply reduced to a description based upon a cross-sectionally averaged streamwise velocity and a representative flow depth.

Direct field observations of such catastrophic motions are extremely difficult to make; in fact there are only a limited number of observations that would permit a partial verification of theoretical models (Gubler 1987, 1989; Norem *et al.* 1986, 1988). In addition, comparison of models with results from field events is often aggravated because these events can be extremely complex in terms of the kinds and sizes of materials that are present as well as the bed and avalanche geometries that might be involved. Laboratory experiments permit a control of both material properties and bed geometries, and thus facilitate comparison of theory with experiment.

In the hope of isolating the simplicities inherent in the response behaviour of rapidly flowing granular materials, it was decided to perform well-defined laboratory experiments and to compare their results with the findings from model computations. A satisfactory fit of such a theory with laboratory data still does not imply that the theory is adequate to describe large-scale processes in nature. Apart from the idealizations of the laboratory experiment scale effects might falsify the conclusions. However, we are confident that the present formulation is superior to the previous simpler treatments because it examines the problem in a more detailed way than in the past and is at least a step in the direction of treating the full problem. The simplest two-dimensional plane flow problem which entails the main features of avalanche motion from the initiation of motion to final runout when the material comes to rest has already been analysed. Preliminary experiments of a finite mass of gravel moving down an inclined rough plane (Huber 1980) indicated promising behaviour of the proposed model (Savage & Hutter 1989). Further experiments were subsequently conducted relating to the evolution of a finite mass of plastic particles released from rest with a prescribed initial geometry and moving down a chute consisting of a straight inclined portion, a curved part and a horizontal part (Plüss 1987; Hutter *et al.* 1988). These experimental measurements were compared with the theoretical prediction of the temporal evolution of the leading and trailing edge of the pile, its total length and its shape by Savage & Hutter (1989) and Hutter *et al.* (1989), and it was found that agreement between theory and laboratory findings was satisfactory.

The curved part in the above-mentioned chute experiments is relatively short; as a result the curvature effects of the bed cannot be large because the avalanche moves along straight portions over most of its track. It was therefore decided to conduct additional experiments on the motion of a finite mass of granular materials along a smoothly curved chute in order to examine the predictive features of the model equations under such more general situations. These experimental measurements are again compared with the theoretical predictions of the temporal evolution of the leading and trailing edge of the pile, its total length and its shape as before, but the comparison is more detailed and thus gives better indication about the suitability of the formulation. In particular, besides the curvature effects we examine whether a restricted class of approximate, so called similarity solutions can appropriately predict the experimental observations.

Conceptually, the granular material is treated as an incompressible Coulomb-type continuum. The sliding that is permitted to take place along the bed is also modelled by a Coulomb-like rate independent dry friction law. The dynamic equations of balance of mass and momentum are used in a transversely integrated form (with accordingly incorporated boundary conditions). The emerging field equations thus form a set of dynamical equations for the averaged streamwise velocity and the avalanche height as functions of position and time. These equations, written in dimensionless form, are valid under the limited assumption of shallowness or slow spatial variation of the avalanche geometry and the track along which the avalanche is moving. This limit is achieved by a non-dimensionalization and scaling analysis with three different characteristic length scales: L for the longitudinal spread of the pile, H for the depth and R for a typical radius of curvature of the bed profile. The aspect ratio $\epsilon = H/L$ and the non-dimensional characteristic curvature $\lambda = L/R$ appear in the dynamical equations as two ordering parameters. Our equations, which will be quoted from Savage & Hutter (1990) but not derived, are valid for $\epsilon \ll 1$ and $\lambda \lesssim O(\epsilon^{\frac{1}{2}})$.

In §2 the model equations are presented for the reduced model of Savage & Hutter (1990); they will be referred to as the general model equations (GM). We discuss the circumstances in which these equations permit similarity solutions (i.e. solutions for which the shape is preserved, which will be called the equations of the similarity model (SM)). In §3 we then present the experimental test apparatus with which a total of 91 experiments were performed and discuss the experimental procedure and how the motion of a finite mass of a granular material was recorded from initiation to

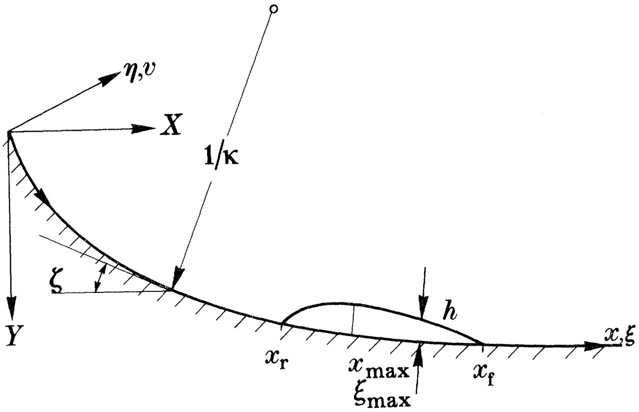

Figure 1. Definition sketch of coordinate system and geometry of a finite mass of granular material moving down a rough curved rigid bed; ξ and η are dimensional coordinates, x and y are dimensionless.

runout. In §4 we describe how the internal angle of friction, ϕ, and the bed friction angle, δ, were measured and how the coefficient of restitution for the various granular materials was estimated. Numerical integration schemes, their accuracy and their reliability are discussed in §5. The comparison of theoretical results and experiments is then presented in §6, while §7 summarizes the findings and presents an outlook to further work.

2. Governing equations

We shall study free surface flow of a granular material along a weakly curved bottom profile (see figure 1). The motion is two dimensional, taking place in vertical planes; the pile of the granular material may start from its rest position and flow down the rough bed until it settles in the runout zone. The bed has a steep slope at the initial position of the pile and gradually approaches a horizontal flat in the downstream direction. Although the material is made up of discrete granules, the body will be treated as a continuum, which implies that the thickness, h, of the sliding and deforming body extends over several particle diameters. Moreover, we shall ignore variations of the density due to void ratio and therefore suppose the incompressibility assumption to be valid to a sufficient degree of accuracy. Observations of our laboratory avalanches through the glass side wall of the confining channel show variations in overall average bulk density from the initiation of motion until the material comes to rest that are typically less than 20%.

Our model equations are based on the following physical statements:

(1) balance laws of mass (in the form of the continuity equation) and linear momentum;

(2) kinematic equation and stress-free boundary conditions at the free evolving surface;

(3) tangency condition of the velocity vector at the basal surface;

(4) constitutive postulates for the material response inside the granular pile and for the sliding mechanism at the bed.

The detailed presentation of these statements is given in Savage & Hutter (1989), here we only elaborate on the constitutive behaviour. As for sliding, a simple

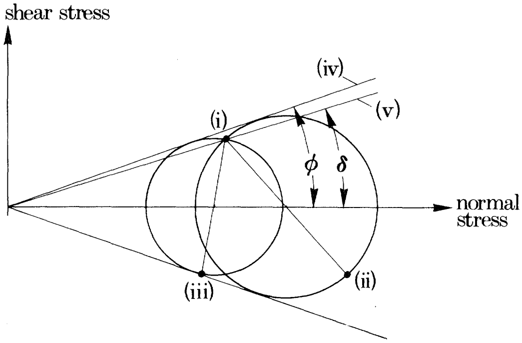

Figure 2. Mohr diagram showing Coulomb yield criterion, bed friction angle, and active and passive stress conditions: (i) $-(p_{\eta\eta}, -p_{\xi\eta})_{\text{bed}}$; (ii) $(p_{\xi\xi}, -p_{\xi\eta})_{\text{bed}}$, passive case; (iii) $(p_{\xi\xi}, -p_{\xi\eta})_{\text{bed}}$, active case; (iv) material yield line; (v) wall yield line.

Coulomb-like dry friction law relates S, the shear traction at the bed, to the normal stress, N, through a local bed friction angle, δ, i.e.

$$S = \pm N \tan\delta, \tag{2.1}$$

where the sign is given by the direction of the sliding velocity. Similarly, if we postulate the granular material to obey a Mohr–Coulomb plastic behaviour with a cohesionless yield, then this yield occurs on a surface element if the shear stress, S, and normal stress, N, acting on this element are related by

$$|S| = N \tan\phi, \tag{2.2}$$

where ϕ is the internal friction angle. We shall not dwell upon a justification of the constitutive postulates (2.1) and (2.2) for flows of granular materials undergoing rapid deformations; this has been done extensively by Savage & Hutter (1989). The relations (2.1) and (2.2) are, however, shown schematically in terms of a standard Mohr diagram in figure 2 for constant δ and ϕ. At the bed, in terms of the coordinates of figure 1, ξ and η, the normal stress $p_{\eta\eta}$ and the shear stress $p_{\xi\eta}$ must be such that they lie on the wall yield line as shown (point (i) in figure 1). As is evident, two possible Mohr circles can be constructed through the point corresponding to the $(p_{\eta\eta}, p_{\xi\eta})$ state. That corresponding to the larger (smaller) value of the normal stress, $p_{\xi\xi} > p_{\eta\eta}$ $(p_{\xi\xi} < p_{\eta\eta})$ is associated with the passive (active) state of stress (to use the common soil mechanics terminology). It will be assumed that active and passive states of stress are developed depending upon whether an element of granular material is being elongated or compressed in the direction parallel to the bed. The stresses parallel and perpendicular to the bed may then be related to each other through an earth pressure coefficient, K_{actpass} as follows:

$$p_{\xi\xi} = K_{\text{actpass}}\, p_{\eta\eta}, \tag{2.3}$$

where K_{actpass} can take active and passive values, K_{act} and K_{pass}. From figure 2 it may easily be shown that

$$\left.\begin{matrix} K_{\text{act}} \\ K_{\text{pass}} \end{matrix}\right\} = 2\left[\frac{[1 \mp \surd(1-\cos^2\phi/\cos^2\delta)]}{\cos^2\phi}\right] - 1, \quad \text{for} \quad \frac{\partial u}{\partial \xi}\left\{\begin{matrix} > 0, \\ < 0. \end{matrix}\right. \tag{2.4}$$

2.1. *The reduced model*

In ensuing developments equations will be written in dimensionless form. Three different length scales, the longitudinal length scale, L, the depth scale, H, and a scale for the radius of curvature of the bed profile, R, will be used. With these, three different (independent) parameters arise, namely the aspect ratio,

$$\epsilon = H/L \ll 1; \tag{2.5}$$

a dimensionless characteristic curvature,

$$\lambda = L/R; \tag{2.6}$$

and the bed friction angle, δ. The following orders of magnitude will be used (Savage & Hutter 1990):

$$\tan\delta = O(\epsilon^{\frac{1}{2}}), \quad \lambda = O(\epsilon^{\frac{1}{2}}). \tag{2.7}$$

Let lengths, curvature, velocity, time and pressure tensor be scaled according to

$$\left.\begin{aligned} (\xi, \eta, \kappa) &= (L\tilde{\xi}, H\tilde{\eta}, \lambda\tilde{\kappa}/L), \\ (u, v, t) &= (\surd(gL)\,\tilde{u}, \quad H\surd(gL)\,\tilde{v}/L, \quad \surd(L/g)\,\tilde{t}), \\ (p_{\xi\xi}, p_{\eta\eta}, p_{\xi\eta}) &= [\rho g H\cos\zeta_0]\,(\tilde{p}_{\xi\xi}, \tilde{p}_{\eta\eta}, \tan\delta\,\tilde{p}_{\xi\eta}), \end{aligned}\right\} \tag{2.8}$$

where quantities having a tilde are dimensionless and are taken to be of order unity and ζ_0 is a characteristic bed slope. Using (2.8) and performing an integration of the balance laws of mass and linear momentum over depth, thereby defining the depth-averaged dimensionless velocity by

$$\bar{u} = \frac{1}{\iota}\int_0^{\iota} \tilde{u}\,\mathrm{d}\eta, \tag{2.9}$$

Savage & Hutter (1990) derive the equations

$$\partial h/\partial t + \partial(h\bar{u})/\partial x = 0, \tag{2.10}$$

$$\frac{\mathrm{d}\bar{u}}{\mathrm{d}t} = \frac{\partial\bar{u}}{\partial t} + \bar{u}\frac{\partial\bar{u}}{\partial x} = \sin\zeta - \tan\delta\,\mathrm{sgn}\,(\bar{u})\,(\cos\zeta + \lambda\kappa\bar{u}^2) - \epsilon K_{\mathrm{actpass}}\cos\zeta\frac{\partial h}{\partial x}, \tag{2.11}$$

in which tildes have been omitted and $\tilde{\xi}$ has been replaced by x, for convenience. The depth-averaged continuity equation (2.10) is exact, but the streamwise momentum equation involves approximations to the extent that terms of higher order than ϵ have been ignored. Equation (2.11) expresses a balance of acceleration (left-hand side) with the streamwise components of the forces (right-hand side). The first term on the right is the contribution of gravity; the second is the basal friction force, consisting of the contribution due to overburden and centrifugal forces and the third term is a longitudinal pressure gradient due to depth variations of the pile.

Provided the angle of friction, δ, between the avalanche and the bed and the basal geometry (in terms of the bed slope, ζ, and the curvature, κ) are known, the temporal evolution of h and $\bar{u}$ can be determined if an initial profile $h(x,0) = h_0(x)$ and depth-averaged velocity distributions $\bar{u}(x,0) = \bar{u}_0(x)$ are prescribed.

When either $\tan\delta$ or λ or both are smaller than order $\epsilon^{\frac{1}{2}}$ and when $\bar{u}$ does not become too large, then the term in equation (2.11) due to the centrifugal effects may be dropped in comparison with the other terms. This does not mean that effects of the curvature of the bed are ignored in this case since ζ may still vary with position and thus incorporate some weak curvature effects implicitly. Both cases will be used

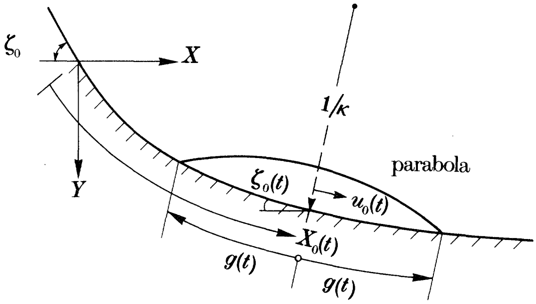

Figure 3. Parabolic shape of the granular avalanche on a weakly curved bed. Shown are an arbitrary position of the centre of mass $x_0(t)$ with velocity $u_0(t)$, semi-length $g(t)$ and the cartesian coordinates X, Y.

below. Moreover, the basal angle of friction, δ, need not be constant and neither will K_{actpass} be in this case. The selection of the earth pressure coefficient $K_{\text{act}}, K_{\text{pass}}$ is made according to whether $\partial \bar{u}/\partial x$ is positive or negative.

2.2. *Similarity solutions*

Savage & Hutter (1989) have found similarity solutions of the equations (2.10), (2.11) for the case of flow of a pile of granular material down a rough inclined flat bed. Savage & Nohguchi (1988), Nohguchi *et al.* (1989) and Hutter & Nohguchi (1989) extended the solution procedure to the same plane flow configuration down rough curved beds having gradually varying slopes. These latter solutions are approximate solutions of (2.10), (2.11) because first, the centrifugal force term in (2.11) was ignored and, second, the variation of the slope angle, ζ, within the moving pile was replaced by a first-order Taylor series expansion about the centre of gravity. The property of the similarity solution is that except for these approximations the parabolic profile is an exact solution of the equations treated by Savage & Nohguchi (1988); these authors also show that the motion of the centre of mass of the parabolic pile and its spread can be derived from a set of ordinary differential equations that must be solved numerically.

Let x_0 and u_0 be the arc length and the streamwise velocity of the centre of mass of the parabolic cap and let X and Y be the cartesian coordinates of this centre as shown in figure 3. Let also g be the semi-length (or semi-spread) of the parabolic pile. Then Savage & Nohguchi (1988) have shown that these variables can be obtained from a solution of the following system of first-order ordinary differential equations:

$$\left.\begin{aligned} \mathrm{d}X/\mathrm{d}t = u_0 \cos\zeta(x_0), \quad \mathrm{d}Y/\mathrm{d}t = u_0 \sin\zeta(x_0), \quad \mathrm{d}x_0/\mathrm{d}t = u_0, \\ \mathrm{d}u_0/\mathrm{d}t = \sin\zeta(x_0) - \tan\delta\cos\zeta(x_0), \quad \mathrm{d}g/\mathrm{d}t = f, \\ \mathrm{d}f/\mathrm{d}t = (2\epsilon/g^2)\,K_{\text{actpass}}\cos\zeta(x_0) + \lambda\kappa(x_0)\,g\cos\zeta(x_0). \end{aligned}\right\} \tag{2.12}$$

These equations hold under the assumptions mentioned above and must be solved subject to the initial conditions that X, Y, x_0, u_0, g and f be prescribed at $t = 0$. A start from rest may be described by the initial conditions

$$X = Y = x_0 = u_0 = f(t_0) = 0, \quad g(0) = d, \tag{2.13}$$

corresponding to an initial semi-length of the parabolic cap of size d. Often $d = 1$; if this choice is taken then $\epsilon = H/L$ is the aspect ratio of the initial pile.

The similarity solution permits deduction of an important and well-known result that can be obtained without recourse to explicit calculations. For constant bed friction angle, an avalanche comes to rest at a position x_0 that is the intersection of the real bed topography with a straight line through the starting point having the inclination angle δ. This inclination is known among avalanche dynamicists and geologists as the 'Pauschalgefälle'.

3. Experimental set-up

In this section, the laboratory test apparatus and the experimental procedures will be described. Only a brief description will be given as details can be taken from Koch (1989).

3.1. *The laboratory test apparatus*

Experiments were performed in a 100 mm wide chute of variable length somewhat greater than 4000 mm. The basal surface of the chute was made of a flexible strip of Makrolon (a material similar to plexiglass but softer and more flexible). This bed could be formed to follow the trace of a prescribed function, in our case two different exponentials with different initial slope angles.

This strip was mounted on a vertical plywood wall of 4000 mm × 2045 mm dimension that itself was coated by an off-white plastic folio. The front wall of the arrangement was made of clear and transparent plexiglass through which the moving granular pile could be photographed. This set-up permits a relatively easy change of the chute geometry; however, we shall only report about experiments of avalanches following the two exponential beds mentioned above. A finite mass of dry granular material was confined by a plate, initially oriented vertically. The granular material was released from rest by quickly rotating the confining plate, thus permitting the granular material to move down the incline. The position of the confining plate can be arbitrarily chosen along the chute, thus allowing a certain variation in the chute geometry without changing the basic arrangement. The motion of the pile of granular material could be observed through the transparent front wall, and it was video-filmed and photographed by a 50 mm camera with a high-speed motor drive capable of operating at nominally 6, 12.5 and 15 frames per second, respectively. The distance of the camera from the chute varied from 3.5 to 5 m, depending on the kind of granules that were used. Generally, the camera was positioned as close to the chute as possible, its minimum distance being dictated by the requirement that the chute could be photographed in its entire length. A clock, accurate to 0.01 s was also positioned such that it was visible on the photographs. Figure 4 gives a sketch of the laboratory test apparatus, figure 5 shows the chute with the bed made of Makrolon and the distance scale that was taped on the front plexiglass wall. Figure 6*a* is a photograph of the plate confining the granular material with its rotating mechanism, while figure 6*b* shows it in operation when 3 l of plastic beads are released.

The tests were performed with seven different sorts of granular materials: (i) nearly spherical glass beads of, respectively 3 and 5 mm diameter, (ii) plastic particles (Vestolen) of lens-like shape having a diameter of 4 mm and a height of 2.5 mm, (iii) two fractions of a quartz granulate having roundish shape and mean diameters of 3 and 5 mm and (iv) two fractions of marmor granules with rougher shapes and the same typical diameters. The material mass densities and the bulk densities corresponding to the densest particle packing are listed in table 1 together with other properties typical for the respective particles that will be described below.

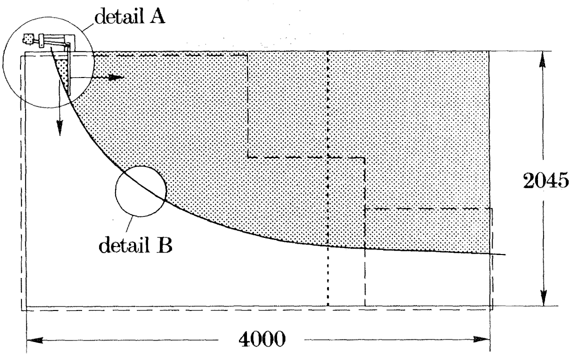

Figure 4. Overview of the laboratory test apparatus showing the dimensions of the back wall and the front plexiglass wall. The basal surface of the chute follows an exponential curve. Dimensions are in millimetres. The details A and B are shown in figures 5 and 6*a*, *b*.

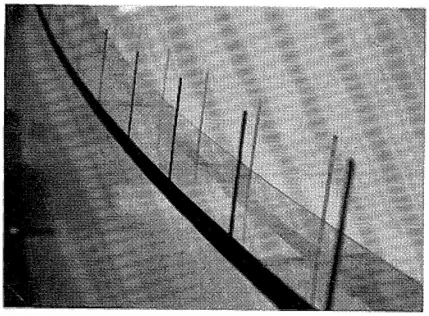

Figure 5. Chute made of Makrolon (a kind of plexiglass, but softer). Visible on the front plexiglass wall is the distance scale.

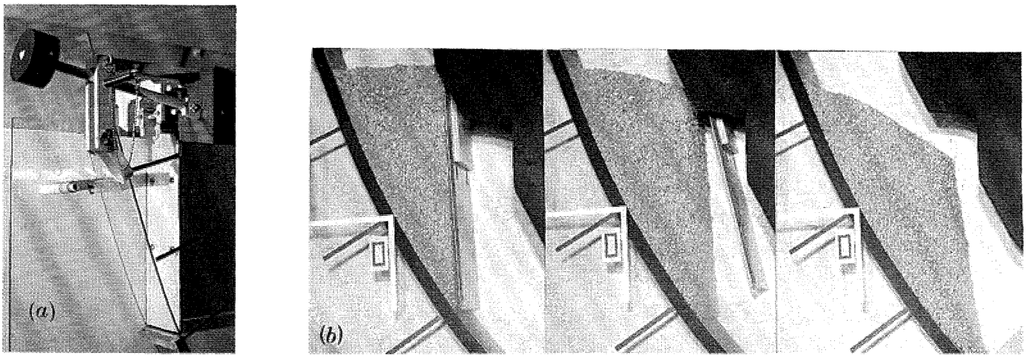

Figure 6. (*a*) Detail A in figure 4 showing the vertical plate confining the granular material. By pulling the bolt, the plate rotates about a horizontal axle in the counter-clockwise direction. (*b*) The release of 3 l of granular material in a chute having 60° initial slope angle. The nominal speed with which the shots were taken was 15 frames per second.

Photographs of the seven different sorts of particles are shown in figure 7. These materials differ by important physical properties: quartz has a high mass density as well as a large internal angle of friction; alternatively, the glass beads have a similarly high mass density but a small internal angle of friction. On the other hand, the plastic particles have a small mass density and an internal angle of friction which

Table 1. *Material constants of all granular materials*

(In this table, d is the mean grain diameter; $l_{\max}$ is the maximum length of a grain found in a sample of *ca.* 200 particles; ρ_1 and ρ_2 are bulk densities, ρ the true density; δ_1, δ_2, δ_3 are the bed friction angles on a bed-lining Makrolon, drawing-paper and sandpaper and e_1, e_2, e_3 the corresponding coefficients of restitution. δ_0 and k_{wall} were determined for a bed-lining Makrolon; compare main text for the definition of δ_0.)

			density			internal angle of friction	bed friction angle					coefficient of restitution		
granulate	d/mm	$l_{\max}$/mm	$\rho_1/(\text{g l}^{-1})$	$\rho_2/(\text{g l}^{-1})$	$\rho/(\text{g l}^{-1})$	ϕ/deg	δ_1/deg	δ_2/deg	δ_3/deg	δ_0/deg	κ_{wall}/deg	e_1	e_2	e_3
glass 0	3	3.7	1784	1632	2730[a]	31.0	20.5	22.0	23.5	18.5	9.0	0.85	0.48	0.67
± (3 mm)			15			2.0	1.5	1.5	1.0		2.0	0.03	0.03	0.05
glass 1	5	5.4	1619	1574	2730[a]	29.0	20.0	—	—	17.5	11.0	0.74	—	—
± (5 mm)			10			1.5	2.0				2.0	0.03		
Vestolen	4	4.0	552	540	540[a]	37.0	23.0	23.5	36.0	17.5	11.0	0.75	0.61	0.54
±			10			2.0	2.0	1.0	2.0		2.0	0.03	0.04	0.06
quartz 0	3	5.0	1562	1426	2600	44.0	25.5	30.5	39.5	21.0	12.0	0.79	0.54	0.7
±			20		150	2.5	2.0	1.5	2.0		2.0	0.03	0.04	0.1
quartz 1	5	8.0	1572	1418	2600	43.0	25.0	28.0	—	21.1	11.5	0.72	0.58	—
±			15		150	3.0	1.5				2.0	0.04	0.05	
marmor 0	3	5.5	1447	1342	2500	47.0	27.0	—	—	22.3	12.5	0.74	—	—
±			40		200	3.0	1.5				2.0	0.03		
marmor 1	5		1495	1334	2500	45.5	26.0	—	—	21.7	12.0	0.68	—	—
±			35		200	4.0	1.0				2.0	0.03		

[a] Provided by the producer.

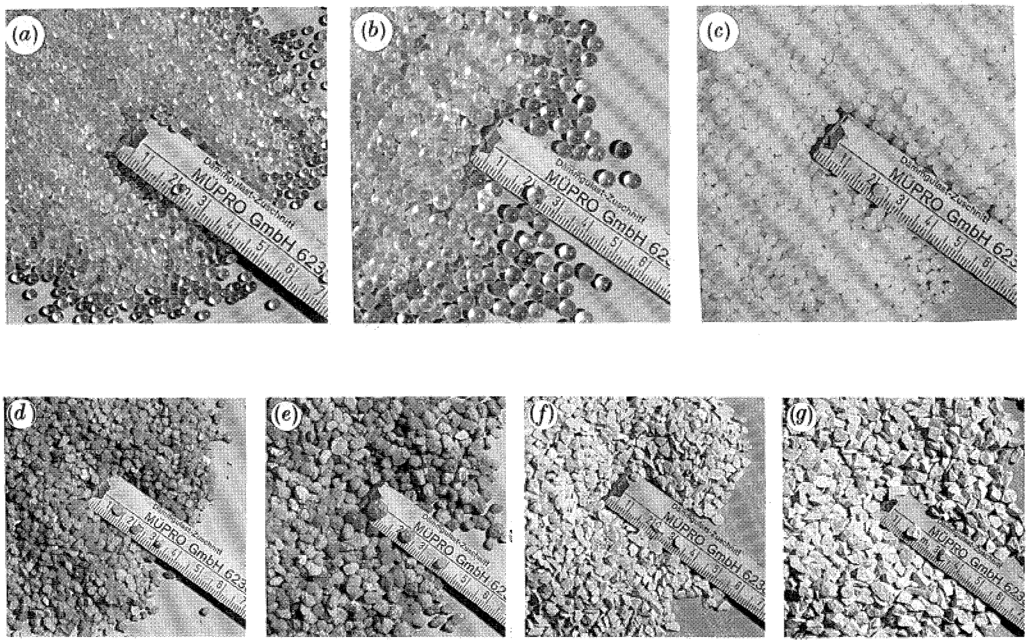

Figure 7. Samples of the granular materials: (*a*) glass 0 (3 mm); (*b*) glass 1 (5 mm); (*c*) Vestolen; (*d*) quartz 0 (3 mm); (*e*) quartz 1 (5 mm); (*f*) marmor 0 (3 mm); (*g*) marmor 1 (5 mm).

lies between those of the quartz and those of the glass beads. Finally, all these materials differ considerably in their coefficient of restitution.

The effects of bed roughness were examined by performing experiments with different bed linings of Makrolon, drawing-paper and no. 120 SIA sandpaper, respectively. In all these cases the side wall smoothness was kept small in an attempt to maintain the flow two dimensional as far as possible.

3.2. *Experimental procedure*

A total of 91 experiments were conducted by varying the following parameters.

1. Bulk volume of the material at its densest packing: 1.5, 2.5 and 3.0 l, and other volumina in special cases.

2. Initial geometry of the pile: three shapes were used, one wedge-like, another one roof-like and a third one nearly in the form of a parabola, but it turned out that the initial shape of the pile had relatively little influence upon the development of the avalanche at later times. Later experiments were conducted with wedge-like initial shapes.

3. The seven different sorts of granular materials: glass 0 and glass 1, Vestolen (plastic beads), quartz 0 and quartz 1, and marmor 0 and marmor 1.

4. Basal bed linings consisting of Makrolon, drawing-paper and no. 120 SIA sandpaper.

5. Two different exponential forms of the chute: in the dimensionless coordinate x (equal to arc length), the slope angle, ζ, is expressed as

$$\zeta(x) = \zeta_0 \exp(-ax), \quad a = 0.1, \tag{3.1}$$

where ζ_0 is the initial slope angle that was chosen to be 60° and 54°, respectively.

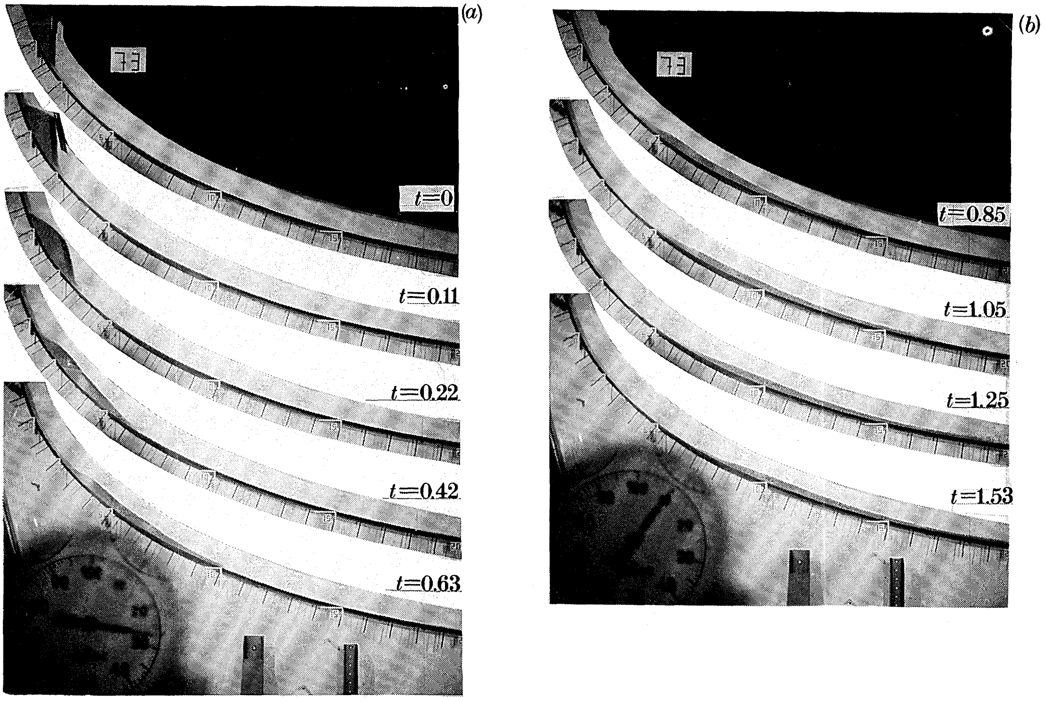

Figure 8. Series of photographs (experiment 73) taken at different dimensionless times of a granular material (3 l of quartz 0 particles) moving down the exponentially curved chute, the bed of which is roughened by drawing-paper and the initial slope angle is 60°.

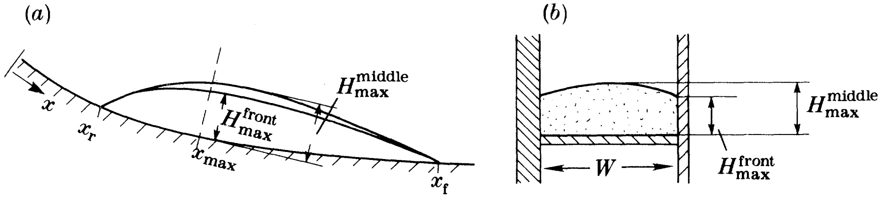

Figure 9. (*a*) Sketch of the front view of the avalanche geometry during motion. The coordinate x is the arc length measured along the base of the chute; x_r, x_f and x_{max} denote the position at the rear end, front end and where the avalanche depth is at a maximum. (*b*) Cross-sectional view of the granular avalanche at the position x_{max}, identifying H_{max}^{middle} and H_{max}^{front}.

Most experiments were performed twice and repeated when mechanical or photographic failures occurred. Results from such experiments differed little, from each other in general, when experiments were instantly repeated but could show considerable deviations when repetitions were done after other experiments had been conducted with the same arrangement. The reason for this behaviour was the fact that the bed-lining Makrolon and to a lesser extent also drawing-paper changed the roughness with the number of experiments. Once this was realized, the bed friction angle, δ, was repeatedly determined, and it was found that, after a certain number of experiments had been performed, it varied with position, see §4.

Typical results of a test run may be seen in figure 8. It shows prints of consecutive shots that are approximately 0.11 s apart of a moving and deforming pile of quartz 0 granules from its initiation to its rest. Such photographs (in large prints) can be used to determine the evolution of the geometry of the granular avalanche as it moves down the curved chute; however, rather than tracing the entire geometry in each print, we have, in general, been satisfied with the following set of variables (see figure 9*a*): x_r, rear end of the pile as a function of time; x_f, front end of the pile as a function of time; $x_{\max}$, position, where the moving pile is thickest as a function of time; $H_{\max}$, height of pile at the position of $x_{\max}$ as a function of time.

Error bounds were also estimated and will be indicated in the analysis below. Because the moving pile becomes longer with increasing time, and readings therefore become more difficult to take from photographs, these error bounds become larger with the distance travelled by the pile. In addition, determination of x_f was less reliable than that of x_r owing to the bigger saltation activity of the particles at the front and, for the marmor grains, because the avalanche front was hidden behind a dust cloud of abraded material. Furthermore, because the depth of the granular pile is bent across the chute as indicated in figure 9*b*, estimates of $H_{\max}$ are necessarily fraught with this uncertainty. Needless to say, estimates for values of $x_{\max}$ must have a large scatter because the depth of the granular avalanche is nearly constant over a large distance. For the settled granular mass, the above quantities were also read directly from the chute and independently recorded. From these readings, which are far more detailed and also more accurate, the following inferences were drawn. Owing to the friction effects of the side wall, the rear end of the granular pile was parabolically distributed across the width of the chute (see figure 10*a*); x_r was identified with the vertex of the 'parabola' in the middle portion of the chute where there remained at least two particle layers. On the other hand, x_r as taken from the prints coincided with the edge of the parabola, these values thus being systematically smaller (up to 4 cm) than the corresponding vertex values. Similarly, at the front, the settled particles are spread over wide distances, see figure 10*b*. In the direct observations, the position of the front of the settled granular mass, x_f, was identified with the position where the chute was covered over half of its width by two particle layers; this resulted in considerably smaller values of x_f than those determined from the photographs. Readings of $H_{\max}$ from the photographs are also systematically bigger than those that were directly read from the settled mass. Mean and maximum differences are as shown in table 2. Evidently, these differences are particularly large for x_f and $x_{\max}$. Moreover, because the deviations are systematical for x_f and $H_{\max}$ and direct readings are more accurate and thus more reliable, the data obtained from the prints must be corrected for these deviations. This was done as follows:

$$x_f^c(t) = x_f^p(t) - \Delta x_f \, dx_f(t)/dx_f(T). \tag{3.2}$$

Here x_f^c, x_f^p and Δx_f are the corrected position of the front, the position of the front obtained from the photographs and the difference in the readings of x_f of the settled granular mass as taken from the photographs and from direct observations, respectively. Furthermore, $dx_f(t)$ is the error bound 'observed' in the photograph taken at time t, and T is the total travel time from initiation to settling. The corrections (3.2) were applied to all variables of table 2 except $H_{\max}$. Henceforth, unless otherwise stated, all variables will be understood to be referred to their corrected values.

Among the more difficult variables that had to be determined experimentally are the time of the onset of the motion ($t = 0$) and that at which the granular pile comes to rest ($t = T$). The former can best be determined by using close-ups of video films

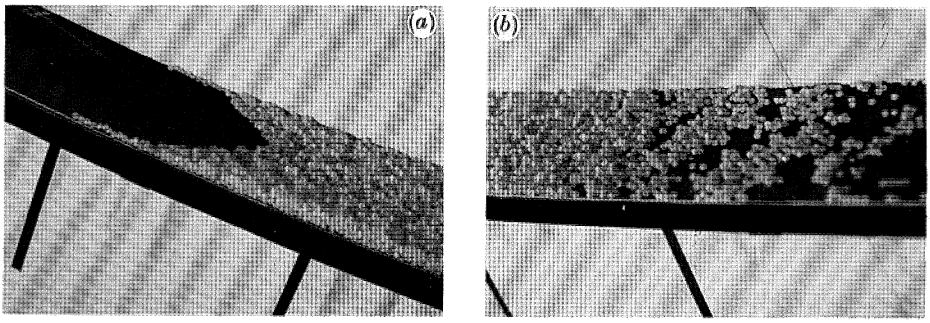

Figure 10. (*a*) Photograph of the rear end of the granular avalanche (experiment 73) at rest, showing the parabolic-type distribution of the rear end across the width of the chute. (*b*) Leading edge of the settled granular avalanche for experiment 73, showing the large spread of the particles.

of the shutter confining the granular material. Under the assumption that the opening of the plate takes place with a constant rotation speed (see figure 6*b*) the time of the opening of the shutter can be extrapolated backwards from the two consecutive frames with non-trivial positions of the plate, taking into account that the video camera was operating at a nominal speed of 25 frames per second. This procedure determined the origin of the time; in this article it is shifted to $t = 0$, and all times of the subsequent photographs were then computed with the aid of the co-revolving clock, the accuracy being ±0.02 s.

Observations indicate that the granules at the rear end of the avalanche come to rest last. Thus the time at which the granular pile comes to rest will be defined as the time when the particles at x_{r} come to rest. This is, in general, not the time at which the photographs were taken. The following procedure permitted its determination, see figure 11. From the three prints before the last rest position, the three positions $x_{\mathrm{r}}(t)$ can be determined, and a polynomial fit through these points will define a continuation $x_{\mathrm{r}}(t)$ for larger times. The rest position of the rear end is also known and defines a horizontal line in figure 11 of which the intersection point with the extrapolated curve will yield an approximation to the time T. This time must lie between those of the two very last photographs of the respective series.

Having determined the positions x_{r}, $x_{\max}$ and x_{f} at the times when the photographs were taken, we can assign velocities to these points as follows:

$$\left.\begin{array}{ll} u_0 = 0, & t = 0, \\ u_i = \tfrac{1}{2}\{(x_{i+1}-x_i)/(t_{i+1}-t_i)+(x_i-x_{i-1})/(t_i-t_{i-1})\}, & i = 1, 2, \ldots, n-1, \\ u_n = (x_n-x_{n-1})/(t_n-t_{n-1}), & t = T. \end{array}\right\} \qquad (3.3)$$

Here the index i denotes the ith photograph and x_i as well as u_i stand for x_{r}, $x_{\max}$, x_{f} and $u(x_{\mathrm{r}})$, $u(x_{\max})$, $u(x_{\mathrm{f}})$, respectively. In equation (3.3) the velocity u_n is less accurate than u_i for $i \leqslant n-1$. Because the x_is are known to within an error Δx_i and also t is known to within an error Δt, these measurement errors are propagated to the velocities and can easily be quantitatively calculated with the aid of equation (3.3). In subsequent graphs the error bars in the velocity plots will also be shown.

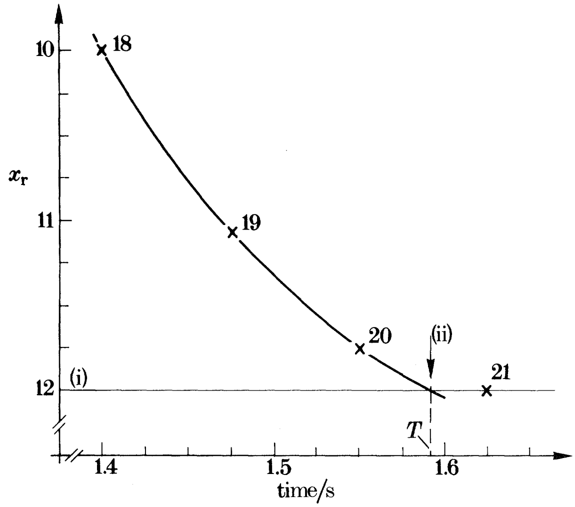

Figure 11. Illustration explaining the determination of the total travel time, T, of the avalanche. The points labelled 19 to 21 show the rear position of the granular avalanche as taken from the photographs, number 21 being the first that shows the avalanche at rest. The arrow marks the travel time, T, as extrapolated from the data. At (i) position x_r in settling zone; at (ii) x_r at rest.

Table 2. *Mean and maximum differences between readings as taken from prints and direct observations*

(A positive sign means that readings from the prints are the larger ones.)

measured quantity	mean difference Δ/mm	maximum difference Δ_{max}/mm
x_r	-20	-40
x_f	$+130$	$+200$
x_{max}	± 60	± 100
H_{max}	$+3$	$+5$

3.3. *An example: experiment* 73

We shall now illustrate the above procedure with experiment 73. It constitutes a mass of nominally 3 l of quartz 0 particles released from rest on an exponential bed with initial slope $\zeta_0 = 60°$ and a bed lined with drawing-paper. A series of photographs of the moving and deforming granular pile has been shown in figure 8. The values of x_r, x_f, x_{max} and H_{max} and the velocities u_r, u_f and u_{max} as determined with the aid of equation (3.3) are collected in table 3 together with the times when the photographs were taken and with the absolute errors of these quantities. At the bottom of the table the values of x_r, x_f, x_{max} and H_{max} are also listed that were read from the settled granular mass. The dimensionless counterpart is shown in table 4; thereby the scales $L = 15$ cm and $H = 15$ cm were used and the corrections explained in (3.2) were implemented. Figure 12*a* shows the graphs of x_r, x_{max}, x_f against time (all dimensionless) including error bars and with/without the corrections (equation (3.2)); these corrections are not visible for x_r. Similarly, figure 12*b* shows the corresponding evolution of the avalanche length, and figure 12*c* those of the velocities all with error bars and with/without corrections (3.2). We have also traced

Table 3. *Values of* x_r, x_f, $x_{\max}$, *maximum avalanche depth* $H_{\max}$ *and* u_r, u_f, $u_{\max}$ *as determined from photographs together with time, t and error bounds*

(At the bottom row the values of x_r, x_f, $x_{\max}$ and $H_{\max}$ are also listed as directly read from the deposition of the granular avalanche in the chute. Data is from experiment 73.)

t/s	x_r/cm	x_f/cm	$x_{\max}$/cm	$H_{\max}$/cm	u_r/(m s^{-1})	u_f/(m s^{-1})	$u_{\max}$/(m s^{-1})
0.00	-23 ± 1	15 ± 0	-18 ± 1	15.0 ± 1	0.00 ± 0.00	0.00 ± 0.00	0.00 ± 0.00
0.01	-23 ± 1	16 ± 1	-16 ± 1	15.0 ± 1	0.43 ± 1.31	1.00 ± 0.54	1.43 ± 1.46
0.11	-19 ± 1	26 ± 1	-3 ± 2	14.5 ± 1	0.60 ± 0.13	1.19 ± 0.09	1.48 ± 0.18
0.22	-10 ± 1	41 ± 1	15 ± 2	11.0 ± 1	0.98 ± 0.18	1.82 ± 0.15	1.43 ± 0.19
0.32	1 ± 1	63 ± 2	27 ± 2	8.5 ± 1	1.18 ± 0.25	2.48 ± 0.22	1.18 ± 0.20
0.42	14 ± 1	90 ± 2	38 ± 2	7.5 ± 1	1.13 ± 0.28	2.55 ± 0.26	1.10 ± 0.25
0.53	25 ± 2	117 ± 3	50 ± 4	6.2 ± 1	1.07 ± 0.35	2.47 ± 0.33	1.12 ± 0.35
0.63	37 ± 2	143 ± 4	62 ± 4	5.0 ± 1	1.19 ± 0.47	2.58 ± 0.44	1.39 ± 0.45
0.74	50 ± 3	172 ± 5	80 ± 6	4.5 ± 1	1.33 ± 0.60	2.56 ± 0.54	1.39 ± 0.55
0.85	65 ± 3	198 ± 6	92 ± 6	4.5 ± 1	1.21 ± 0.68	2.44 ± 0.65	1.22 ± 0.65
0.95	75 ± 3	222 ± 7	105 ± 7	4.0 ± 1	0.95 ± 0.73	1.80 ± 0.77	1.05 ± 0.71
1.05	84 ± 4	234 ± 8	113 ± 7	4.0 ± 1	1.02 ± 0.87	1.79 ± 0.87	1.11 ± 0.76
1.15	96 ± 5	259 ± 9	128 ± 8	4.0 ± 1	1.17 ± 1.04	1.89 ± 0.97	1.81 ± 0.87
1.25	108 ± 5	273 ± 10	150 ± 9	4.0 ± 1	0.83 ± 1.04	1.06 ± 1.03	1.51 ± 0.91
1.36	113 ± 5	281 ± 11	159 ± 9	4.0 ± 1	0.38 ± 1.02	0.76 ± 1.12	0.51 ± 0.91
1.46	116 ± 5	289 ± 12	161 ± 9	4.0 ± 1	0.29 ± 1.39	0.76 ± 1.67	0.24 ± 1.29
1.53	118 ± 6	294 ± 15	163 ± 12	4.0 ± 1	0.00 ± 0.00	0.00 ± 0.00	0.00 ± 0.00
settling down zone							
0.00	119 ± 1	277 ± 2	160 ± 10	3.5 ± 0			

Table 4. *As table 3 but with all quantities made dimensionless with the scales introduced in §2*

(All values of x_r, x_f and $x_{\max}$ are corrected as described in the main text.)

t/s	x_r/cm	x_f/cm	$x_{\max}$/cm	$H_{\max}$/cm	u_r/(m s^{-1})	u_f/(m s^{-1})	$u_{\max}$/(m s^{-1})
0.0	-1.5 ± 0.0	1.0 ± 0.0	-1.2 ± 0.1	1.00 ± 0.033	0.00 ± 0.00	0.00 ± 0.00	0.00 ± 0.00
0.1	-1.5 ± 0.0	1.0 ± 0.0	-1.1 ± 0.1	1.00 ± 0.033	0.35 ± 1.08	0.59 ± 0.33	1.17 ± 5.01
0.9	-1.3 ± 0.0	1.7 ± 0.0	-0.2 ± 0.1	0.97 ± 0.033	0.50 ± 0.11	0.96 ± 0.08	1.22 ± 0.61
1.7	-0.7 ± 0.0	2.6 ± 0.1	0.9 ± 0.1	0.73 ± 0.033	0.81 ± 0.15	1.45 ± 0.12	1.18 ± 0.65
2.5	0.1 ± 0.1	4.1 ± 0.1	1.8 ± 0.1	0.57 ± 0.033	0.97 ± 0.20	1.99 ± 0.18	0.96 ± 0.69
3.4	0.9 ± 0.1	5.8 ± 0.1	2.5 ± 0.1	0.50 ± 0.033	0.93 ± 0.23	2.06 ± 0.22	0.88 ± 0.86
4.2	1.6 ± 0.1	7.6 ± 0.2	3.3 ± 0.2	0.41 ± 0.033	0.88 ± 0.29	1.95 ± 0.27	0.90 ± 1.19
5.1	2.4 ± 0.1	9.2 ± 0.3	4.1 ± 0.3	0.33 ± 0.033	0.98 ± 0.39	2.02 ± 0.36	1.13 ± 1.54
6.0	3.3 ± 0.2	11.1 ± 0.3	5.2 ± 0.4	0.30 ± 0.033	1.09 ± 0.50	2.04 ± 0.44	1.13 ± 1.88
6.8	4.3 ± 0.2	12.8 ± 0.4	6.0 ± 0.4	0.30 ± 0.033	1.00 ± 0.56	1.92 ± 0.54	1.00 ± 2.22
7.6	5.0 ± 0.2	14.3 ± 0.5	6.9 ± 0.4	0.27 ± 0.033	0.78 ± 0.61	1.37 ± 0.63	0.86 ± 2.44
8.5	5.6 ± 0.3	15.0 ± 0.5	7.4 ± 0.5	0.27 ± 0.033	0.84 ± 0.72	1.38 ± 0.71	0.90 ± 2.60
9.3	6.4 ± 0.3	16.6 ± 0.6	8.4 ± 0.5	0.27 ± 0.033	0.97 ± 0.85	1.47 ± 0.80	1.48 ± 2.98
10.1	7.2 ± 0.3	17.4 ± 0.7	9.9 ± 0.6	0.27 ± 0.033	0.68 ± 0.86	0.79 ± 0.84	1.23 ± 3.14
11.0	7.5 ± 0.3	17.9 ± 0.7	10.5 ± 0.6	0.27 ± 0.033	0.31 ± 0.84	0.54 ± 0.92	0.42 ± 3.14
11.8	7.7 ± 0.3	18.4 ± 0.8	10.6 ± 0.6	0.27 ± 0.033	0.24 ± 1.15	0.38 ± 1.37	0.16 ± 4.42
12.4	7.9 ± 0.4	18.5 ± 1.0	10.7 ± 0.8	0.27 ± 0.033	0.00 ± 0.00	0.00 ± 0.00	0.00 ± 0.00
settling down zone							
0.00	7.9 ± 0.1	18.5 ± 0.1	10.7 ± 0.7	0.23 ± 0.010			

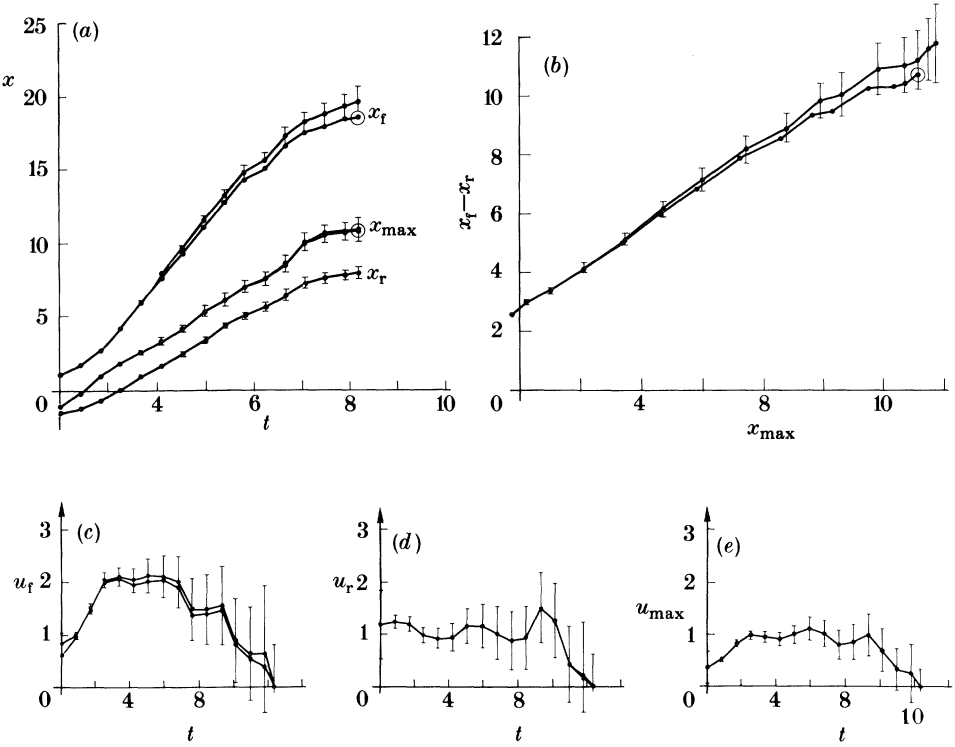

Figure 12. (*a*) Temporal evolution of the dimensionless positions x_r, x_f and x_{max} for experiment 73, as read from photographs with estimates for error bars. Shown are also the corrected positions (without shifted error bars) as described in the text. (*b*) Dimensionless avalanche length, $x_f - x_r$, plotted against dimensionless x_{max} as deduced from the results shown in (*a*) with error bars and corrected. (*c*) Dimensionless frontal velocity u_f, (*d*) velocity at x_{max}, u_{max}, and (*e*) rear velocity u_r, plotted against time for experiment 73 as deduced from the photographs including error bars and corrected as described in the text.

Table 5. *Time, volume and its error as determined from the photographs shown in figure 8*

(The nominal volume at densest packing was 3 l, the mean value here is $V = 3.75$ l and the standard deviation from this mean is 0.0703.)

time/s	volume/l	Δ	Δ^2
0.00	3.51	−0.24	0.0576
0.11	3.44	−0.31	0.0961
0.22	3.65	−0.10	0.0100
0.42	4.20	+0.45	0.2025
0.63	3.97	+0.22	0.0484
0.85	3.70	−0.05	0.0025
1.05	4.08	+0.28	0.0784
1.25	3.65	−0.10	0.0100
1.53	3.51	−0.24	0.0576
	3.75		0.5631 : 8
			$\sigma^2 = 0.0703$

the contours of the geometry of the piles in the photographs and determined the sizes of the respective volumes. Table 5 contains these values including their mean and standard deviation; these results give an indication as to the validity of the assumption of incompressibility. Evidently this assumption is not strictly satisfied. In particular the bulk material seems to experience a dilation of approximately 20% at the immediate start of the motion. Subsequently the incompressibility assumption is reasonably satisfied, however.

4. Measurement of phenomenological coefficients

The theoretical formulation of §2 requires the values of the internal friction angle, ϕ, and the bed friction angle, δ; these were experimentally determined for all materials together with some estimates of the coefficient of restitution.

4.1. *Internal friction angle*

The static internal angle of friction is generally identified with the angle of repose of a wedge-type pile of the granular material that is deposited on a horizontal plane. The wedge-type piles were formed on a horizontal plate that was roughened by sandpaper and confined by two parallel smooth styropor walls, see figure 13*a*. Simply pouring the granules from above into the confined space resulted in a bell-shaped pile, see figure 13*b*. Forms closer to wedges were obtained if some particles at the basal wedges were removed and the particles at the free surface were allowed to rearrange their position, see figure 13*c*. The internal angle of friction was then determined by measuring the angle of repose in three different ways. The mean angles, α_1 and α_2 between the left and right shoulders of the wedge and the horizontal plane were determined with the aid of a protractor, and the angle $\alpha_3 = \arctan(2H/B)$ was calculated by measuring the height of the wedge and its basal length B. For each material three different piles were made with different total masses. The internal angle of friction was then taken to be the arithmetic mean of the nine determined angles of repose. Results including maximum deviations from this mean are given in table 6.

Dynamic internal friction angles are smaller than their static counterparts. Hungr & Morgenstern (1984*a*, *b*) found in their annular shear cell experiments that the dynamic friction angle was about 4° less than the angle of repose of the granular material. We shall in ensuing computations examine the influence of this reduction. The numerical values in table 6 also tend to be a bit large. For this reason additional experiments were performed by building piles with the forms of circular cones. Corresponding values of the angle of repose tended to be a bit larger than the values in table 6, for which reason these values were taken as acceptable minima. Later computations also indicated that the computed results were not critically sensitive to the values of ϕ except when the bed friction angle, δ, was close to ϕ, so a very accurate determination of ϕ is not so important, even though the reduction to the dynamic value is essential.

4.2. *Bed friction angle*

Another parameter that appears in the theory is the bed friction angle, δ_0. (We use the subscript 0 for reasons that will become apparent later.) Its determination by experiments followed Savage & Hutter (1990) and Hutter *et al.* (1990).

A small container of 70 mm diameter for granular material was made out of paper in the form of a cylinder, the bottom edge surface of which was coated by plastic tape

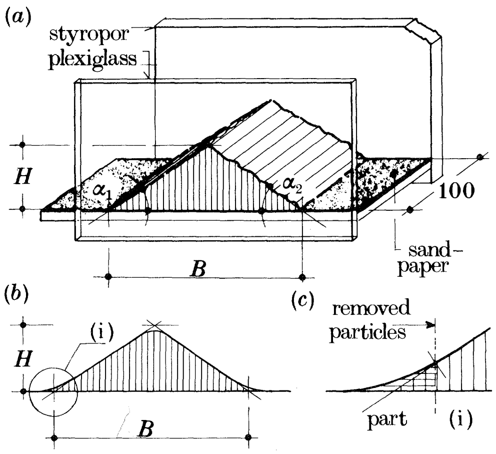

Figure 13. (*a*) Front view through the plexiglass wall showing the bell-shaped pile and its triangular idealization. Dimension is in millimetres. (*b*) Arrangement for measuring the internal angle of friction, ϕ. The basal surface is roughened by sandpaper. To determine ϕ, α_1, and α_2, H and B are measured. (*c*) Removing a few particles at the basal vertex and letting the surface particles rearrange produced piles that were closer to equilateral triangles.

Table 6. *Measured mean static internal angle of friction and maximum deviations in single measurements*

material	ϕ_{mean}/deg	$\Delta\phi$/deg
glass 0	31	2.0
glass 1	29	1.5
Vestolen	37	2.0
quartz 0	44	2.5
quartz 1	43	3.0
marmor 1	47	3.0
marmor 2	46	4.0

for reinforcement and in order to smoothen its edge. A tilting plane apparatus was constructed. Its tilting plate could be lined with the basal bed material of appropriate roughness and inclined at various angles relative to a horizontal board to which it was hinged. The granular material was introduced into the paper cylinder positioned on the tilting plate, the paper ring was subsequently lifted about half a particle diameter to eliminate the contact, and the rough plate was then gradually inclined until a gentle push on the side of the cylinder containing the granular material would result in its continued motion down the incline. The corresponding tilt angle was taken to be the bed friction angle, δ_0, of the theory.

The above measurements were conducted several (generally three to four) times for each granular material and each bed lining. Table 7 contains the mean values including the maximum deviations of the individual measurements from these means.

It has been mentioned that repeated flow of the granular avalanches down the chute wore down the bed and, depending on the bed-lining material, made it smoother or rougher as the number of tests increased. The bed can also become more worn over certain portions, leading to a non-uniform value of δ_0 over the avalanche

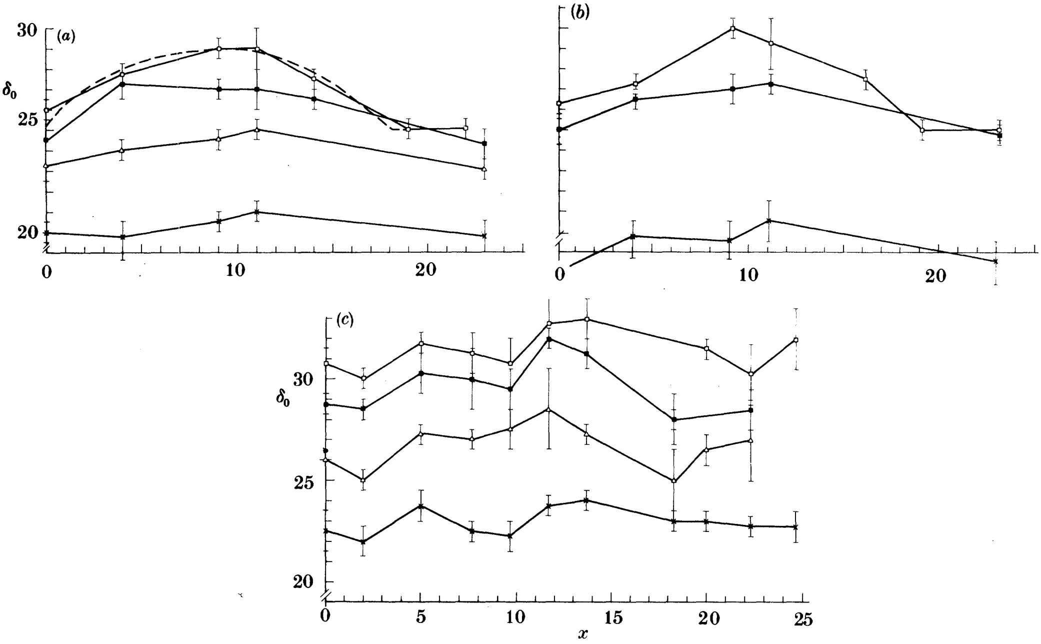

Figure 14. (*a*) Measured bed friction angle as a function of position along the chute for the bed-lining Makrolon after experiment 37, for the materials glass 0, ×—× ; Vestolen, △—△; quartz 0, □—□; and quartz 1, ■—■. The dashed line is the fit (equation (6.1)) to the quartz 0 data. (*b*) Same as (*a*) but for the granular materials glass 1, marmor 0 and marmor 1. (*c*) Measured bed friction angle as a function of position along the chute for the bed-lining drawing-paper after experiment 74, for the materials glass 0, Vestolen, quartz 0, and quartz 1. Legend as for (*a*).

Table 7. *Mean bed friction angle as determined by experiment*

material	δ_0/deg on Makrolon	δ_0/deg on drawing-paper	δ_0/deg on sandpaper
glass 0	20.5 ± 1.5	22.0 ± 1.5	23.5 ± 1.0
glass 1	20.0 ± 2.0	—	—
Vestolen	23.0 ± 2.0	23.0 ± 1.5	36.0 ± 2.0
quartz 0	25.5 ± 1.5	30.5 ± 1.5	39.5 ± 2.0
quartz 1	20.5 ± 1.5	28.0 ± 1.0	—
marmor 0	27.0 ± 1.5	—	—
marmor 1	26.0 ± 1.0	—	—

path. We examined this behaviour and determined the bed friction angle on the worn-out bed as a function of position under the following conditions: (i) after experiment 37 for the bed-lining Makrolon for all granular materials and (ii) after experiment 74 for the bed-lining drawing-paper again for a selection of granular materials. Figure 14 summarizes the results of the measurements. δ_0 is plotted against dimensionless arc length, x. Evidently, for Makrolon, the variation of δ_0 along the bed is concave, and it is more conspicuous for the larger bed friction angles of the granular material. The differences between the largest and smallest values of δ_0 are up to 5° for the material marmor 0, this maximum arising approximately where avalanche velocities are largest. For the material glass 0, these differences are hardly experimentally significant, however. For drawing-paper, the inferences that could be

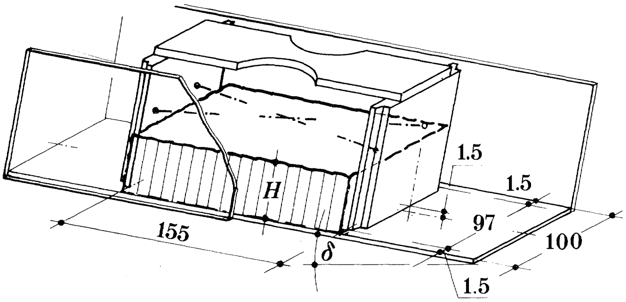

Figure 15. Box with crosswise tightened strings for stabilization, placed between the back and front wall of the chute and positioned on a strip lined with Makrolon. The box is uniformly filled with the granular material to the depth H. The tilting angle, δ, at which the box, including the granular material inside it, commences to move is defined as the effective bed friction angle. Dimensions are in millimetres.

drawn are less conclusive, and it may well be justified to work with a constant bed friction angle. A possible reason could be the kinks in the paper which were unavoidable when the bed was attached to the tilting board. Fortunately, as calculations have shown, the computational results are relatively insensitive to the variations in the bed friction angle.

4.3. *Influence of wall friction*

The theory that was developed in §2 assumes two-dimensional flow conditions and neglects any effects of side wall friction. However, in our experimental arrangement the flow was confined between the side walls of the chute, and these side walls exert shear stresses which additionally slow the flow; evidence of these side wall effects are given in figure 10*a*. A simple approximate way to account for the side friction effects is to make use of an effective bed friction coefficient $\tan\delta_{\text{eff}}$ as suggested by Roberts (1969) and Savage (1979). According to these authors the effective bed friction angle can accurately be expressed as a linear function of the depth to width ratio, namely

$$\delta_{\text{eff}} = \delta = \delta_0(1+k(H/W)\,h) = \delta_0 + \epsilon k_{\text{wall}}\,h, \quad k_{\text{wall}} = (L/W)\,k, \tag{4.1}$$

where H is the characteristic height scale, W is the width and h the dimensionless depth of the flow. (Savage uses a linear relation between $\tan(\delta_{\text{eff}})$ and $\tan(\delta_0)$; however, since corrections are small, this difference relative to equation (4.1) is spurious.) Because W is constant (equal to 100 mm) we have determined k_{wall} (in degrees) by measuring effective bed friction angles δ as explained below and evaluating k_{wall} with the aid of

$$k_{\text{wall}} = (\delta - \delta_0)\,L/H. \tag{4.2}$$

L is the longitudinal scale, chosen to be 150 mm.

To find the effective bed friction angle for the bed-lining Makrolon, a 400 mm long and 100 mm wide Makrolon strip was placed between the back wall and the plexiglass front wall of the experimental apparatus. It was placed such that it could be rotated about its 'footpoint' and the angle of inclination be measured. A box, 97 mm wide, was made from styropor plates and placed between the two walls on the Makrolon strip as shown in figure 15 such that its front and rear wall did not touch the walls of the chute. Crosswise tightened strings enhanced the stability of the box

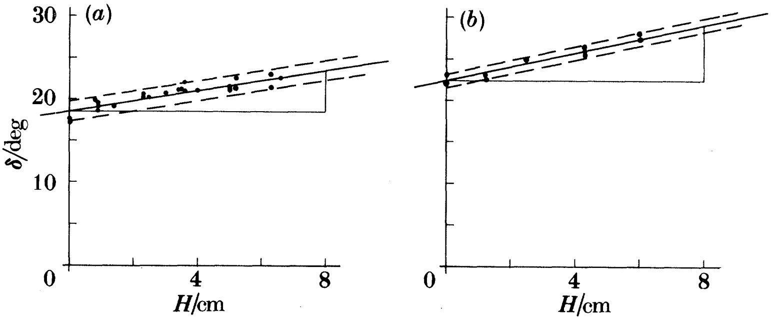

Figure 16. Effective bed friction angle, δ, plotted against depth H (in centimetres) for (*a*) glass 0 on a Makrolon lining and (*b*) marmor 0 granules on a Makrolon lining. Points represent the experimental findings, solid lines give the best fit linear dependence with dashed lines showing the variance. The values of δ_0 and k_{wall} arising in equation (4.1) and the variation $\Delta\delta$ (the indicated band width) are: for (*a*), $\delta_0 = 18.5°$, $\Delta\delta = 1.2°$, $k_{\text{wall}} = 9.19°$; for (*b*), $\delta_0 = 22.3°$, $\Delta\delta = 0.8°$, $k_{\text{wall}} = 12.6°$.

Table 8. *Experimentally determined values of* k_{wall} *for basal surfaces lined with Makrolon*

material	δ_0/deg	κ_{wall}/deg	$\Delta\kappa_{\text{wall}}$/deg (±)	k_{wall}/deg (Savage 1979)
glass 0	18.5	9.0	2.0	0.324
glass 1	17.5	11.0	2.0	0.419
Vestolen	17.5	11.0	2.0	0.419
quartz 0	21.0	12.0	2.0	0.381
quartz 1	20.1	11.5	2.0	0.381
marmor 0	22.3	12.5	2.0	0.374
marmor 1	21.7	12.0	2.0	0.368

and by taping the bottom and side edges of the vertical walls of the box its own friction in motion was reduced. The total mass of the box was 37 g. The space between the box and the Makrolon strip was filled with different masses of the granular material (120 g and 1700 g for the minimum and maximum respectively), uniformly distributed, and the height of the pile was determined. After lifting the box by approximately half a grain diameter, so as to eliminate its contact with the base and the walls, the entire arrangement was gently tilted until the box with its granular mass was set in motion. The corresponding tilt angle was then measured and identified with the effective bed friction angle δ. Figure 16*a*, *b* shows the measured values of δ plotted against H for the glass 0 particles and the marmor 0 granules and a Makrolon strip. Also shown in the figure is the linear least square fit and the width of variation. Table 8 contains all determined values of k_{wall} including their variation as well as values of δ_0 obtained this way.

Note that bed friction angles at zero height, δ_0, are smaller than those of table 7 by several degrees. We suspect that in the first experimental method the height must have affected the numerical values obtained. No definite inferences can be drawn, but a dependence of δ on overburden pressure is likely. The right-hand column of table 8 shows the values of k_{wall} as defined in equation (4.1); these values are comparable in size to similar ones determined by Savage (1979) even though they are slightly smaller.

Table 9. *Bulk densities at the closest packing and their values after shaking the filled cylinder*

material	bulk density $\rho_1/(\mathrm{g\ l^{-1}})$ (dense)	$\rho_2/(\mathrm{g\ l^{-1}})$ (loose)	difference/%
glass 0	1784 ± 15	1632	9
glass 1	1619 ± 10	1574	4
Vestolen	552 ± 10	540	4
quartz 0	1562 ± 20	1426	10
quartz 1	1572 ± 15	1418	10
marmor 0	1447 ± 40	1342	8
marmor 1	1495 ± 35	1334	12

Selective experiments were repeated with the bed linings drawing-paper and granular material quartz 0. It was found that the values of k_{wall} were of the same order of magnitude. Consequently, the experiments were not repeated for the other bed linings, and computations were conducted using the values of table 8.

4.4. *Bulk density*

One further variable entering the theory of §2 is the bulk density of the particles; it was determined for a dense as well as a looser packing. Results are shown in table 9. They were obtained as follows. A measuring cylinder was filled to its 500 ml marking by pouring the granular material from a height between 30–50 cm. The packing obtained this way was defined as being dense. Values of the bulk density for the less dense (or loose) packing were obtained by shaking the measuring cylinder after filling. This resulted in a new volume of the material at the same mass. In the experiment the material behind the confining plate was defined as dense in the above sense.

4.5. *Coefficient of restitution*

The theoretical formulation of §2 does not require knowledge of the coefficient of restitution. Nevertheless it was determined by us as the ratio

$$e = \sqrt{(h_1/h_0)} \tag{4.3}$$

of a particle falling from rest at position h_0 on to a plane and rebounding to a height h_1. We regard e as given in (4.3) as a definition that incorporates, at the moment of impact, elastic/plastic properties of the particle and the bed, as well as those of the shape of the particles. Edgy particles are spread much more to the sides than round particles, and their rebound height might also be determined by the way they interact with the plane during impact. Therefore e, as defined in (4.3), does not only contain information about energy dissipation during impact. None the less, we conjecture that the values of e give information about the fluctuating activity of the particles under avalanching motion. Table 10 lists values of e as obtained with the three different bed linings (subscripts 1, 2 and 3 for Makrolon, drawing-paper and sandpaper, respectively). The listed values are maxima from close to 50 repetitions of the same experiment. The falling particles were video filmed and rebound heights were determined from single frame searches.

All experimentally determined constants and phenomenological coefficients are collected in table 1.

Table 10. *Coefficients of restitution obtained between the indicated particles and a plate lined with Makrolon* (e_1), *drawing-paper* (e_2), *and sandpaper* (e_3)

material	e_1	e_2	e_3
glass 0	0.85 ± 0.03	0.48 ± 0.03	0.67 ± 0.05
glass 1	0.74 ± 0.03	—	—
Vestolen	0.75 ± 0.03	0.61 ± 0.04	0.54 ± 0.06
quartz 0	0.79 ± 0.03	0.54 ± 0.04	0.70 ± 0.10
quartz 1	0.72 ± 0.04	0.58 ± 0.04	—
marmor 0	0.74 ± 0.03	—	—
marmor 1	0.68 ± 0.03	—	—

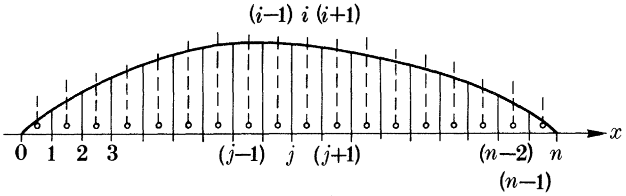

Figure 17. Definition of mesh cell notation for lagrangian numerical scheme. The indices i refer to cell centres, j to cell boundaries.

5. Numerical integration schemes

In the present paper we shall primarily consider the numerical integration of the differential equations (2.10) and (2.11); however, we shall also compare solutions obtained for these with those obtained from the system (2.12), valid for the similarity solutions, in order to examine the validity of the similarity solutions. In this section we shall concentrate upon the reliability of the proposed schemes.

5.1. *Lagrangian numerical scheme for the system* (2.10) *and* (2.11)

Savage & Hutter (1989, 1990), after unsuccessful attempts to find satisfactory numerical solutions for equations (2.10) and (2.11) with a conventional eulerian finite difference scheme, proposed a lagrangian finite difference scheme in which the computational grid is advected with the material particles. Such an approach is a natural choice for the granular avalanche problem which involves the determination of the position of the moving air–granular material interface surface; and it proved to be numerically successful. Thus we follow Savage & Hutter (1989) and extend their analysis by a numerical sensitivity study. In doing so we justify at the same time the reliability of the results.

The granular depth profile is divided into a number of N cells, the boundaries of which are advected with the depth-averaged velocity of the granular material. We use an indexed notation in which i corresponds to the cell centres and j to the cell boundaries as shown in figure 17. The cell boundary points are defined at times $(n-1)$ and designated as x_j^{n-1} the velocities of the cell boundary points are defined at the half-time steps and are expressed as $u_j^{n-1/2}$.

We integrate the depth-averaged conservation of mass equation (2.10) between x_j and x_{j+1}, which after some further manipulation yields

$$\Delta L_i \bar{h}_i = \text{const.} \approx \Delta L_i h_i, \tag{5.1}$$

where
$$\Delta L_i = x_{j+1} - x_j, \tag{5.2}$$

$$\Delta L_i \bar{h}_i = \int_{x_j}^{x_{j+1}} h \, \mathrm{d}\xi. \tag{5.3}$$

The computations proceed as follows. It is assumed that $u_j^{n-1/2}$, x_j^{n-1} and h_i^{n-1} are known (at time $t = 0$ they correspond to the initial values). We obtain the new positions of the cell boundaries x_j^n after an elapsed time Δt by the equation

$$x_j^n = x_j^{n-1} + u_j^{n-1/2} \Delta t. \tag{5.4}$$

The depth at the cell centres, i, is obtained by using equations (5.1) and (5.2); thus

$$h_i^n = h_i^{n-1} (x_{j+1}^{n-1} - x_j^{n-1}) / (x_{j+1}^n - x_j^n). \tag{5.5}$$

The velocities at the cell boundaries may be determined by using the depth-averaged momentum equation (2.11)

$$\begin{aligned} u_j^{n+1/2} = u_j^{n-1/2} + \Delta t [&\sin \zeta_j - \tan \delta \operatorname{sgn} (u_j^{n-1/2}) \\ &(\cos \zeta_j + \lambda \kappa_j^n (\bar{u}_j^{n-1})^2) - \epsilon K_{\mathrm{actpass}}^{j,n} \cos \zeta_j P_j^n], \end{aligned} \tag{5.6}$$

where
$$\begin{aligned} P_j^n &= h_0^n / (x_0^n - x_j^n), & j &= 0, \\ P_j^n &= (h_i^n - h_{i-1}^n) / (x_i^n - x_{i-1}^n), & j &= 1, \ldots, N-1, \\ P_j^n &= (h_N^n - 1) / (x_j^n - x_{N-1}^n), & j &= N \end{aligned}$$

and
$$x_i^n = \tfrac{1}{2}(x_j^n + x_{j+1}^n). \tag{5.7}$$

Here, the bed inclination ζ_j follows the chosen exponential bed profile

$$\zeta_j^n = \zeta_0 \exp(-a x_j^n), \tag{5.8}$$

the curvature term is given by

$$\lambda x_j^n = a \zeta_0 \exp(-a x_j^n), \tag{5.9}$$

for each cell, and the earth pressure coefficient K_{actpass} in each cell is selected according to the rule

$$K_{\mathrm{actpass}}^{j,n} = \begin{cases} K_{\mathrm{act}} \\ K_{\mathrm{pass}} \end{cases} \text{for } \tilde{u}_j + 1 - \tilde{u}_j \begin{cases} \geqslant 0, \\ < 0. \end{cases} \tag{5.10}$$

An artificial viscosity term

$$\psi_j^n = \mu (u_{j+1}^{n-1/2} - 2u_j^{n-1/2} + u_{j-1}^{n-1/2}) / (x_{j+1}^n - x_{j-1}^n)^2 \tag{5.11}$$

was added to the right-hand side of (5.6) inside the bracketed term for the calculation of points other than the leading and trailing edge points. ψ_j^n dampens a possible amplification of the velocity gradients and thus reduces the numerical ripples that tend to develop under certain conditions. More details regarding the justification of the introduction of the numerical diffusion can be found in Anderson *et al.* (1984).

The accuracy of the lagrangian finite difference scheme depends upon the number of cells, N, the step size, Δt, and the artificial viscosity, μ. To examine the influence of these parameters a model avalanche with the following data was analysed:

(1) friction angles: $\phi = 37°$, $\delta = 22°$, $k_{\mathrm{wall}} = 0°$;
(2) bed geometry (3.1) with $\zeta_0 = 60°$, $a = 0.1$;
(3) aspect ratio $\epsilon = 0.5$;

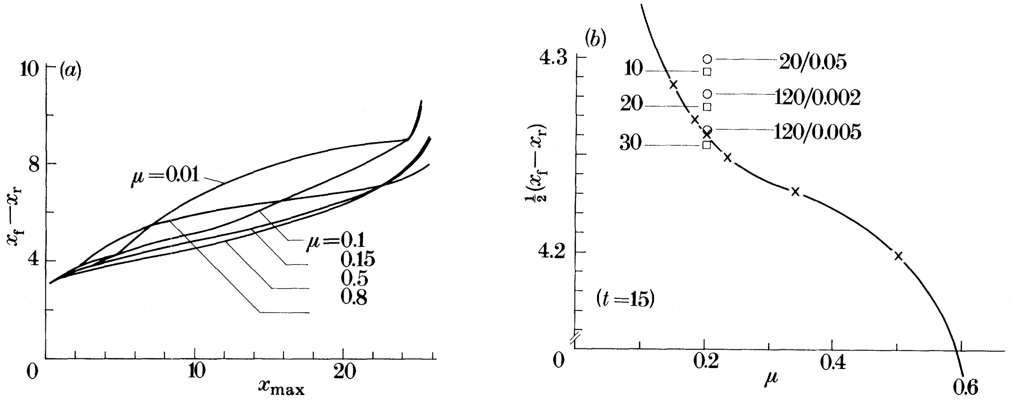

Figure 18. (a) Avalanche length of the model avalanche described in the text plotted against the position x_{max} of maximum height. The different curves are valid for different values of the artificial viscosity, μ. Notice the kinks that occur when μ is below 0.15. (b) Avalanche half-length of the model avalanche described in the text plotted against the artificial viscosity, μ, for the dimensionless time $t = 15$ (immediately before the avalanche comes to rest). The crosses were obtained for computations with $N = 40$ cells and a time step $\Delta t = 0.02$. The open squares hold for $\Delta t = 0.02$, $\mu = 0.2$ and $N = 10, 20, 60$, respectively; the open circles show the length when $\mu = 0.2$ and $(N, \Delta t) = (20, 0.05), (120, 0.002), (120, 0.005)$.

(4) initial geometry of the granular avalanche as shown in the second photograph of figure 8 (experiment 73) with dimensionless rear and front velocities $v_r = 0.65$ and $v_f = 1$, respectively at the dimensionless time $t = 0.9$.

The avalanche length $(x_f - x_r)$ was selected as the representative quantity for the sensitivity study because it turned out that the errors in the computational results were particularly pronounced for this variable.

Computations showed that with small values of the artificial viscosity μ $(\leqslant 0.15)$ the avalanche length plotted as a function of time or x_{max} (as shown in figure 8a) developed kinks. (Notice that our artificial viscosity differs from that used by Savage & Hutter (1989). Their values are obtained by multiplying our values with the value assigned to Δt.) We regard the occurrence of these kinks as an indication of the development of inaccuracies, simply because we do not expect discontinuities to arise in a granular avalanche moving along a very smooth bed. In figure 18a, of which the results were obtained with 40 cells and $\Delta t = 0.02$, the graphs of the avalanche length are very close to each other when $0.15 \leqslant \mu \leqslant 0.5$, but start to deviate from each other again when μ becomes larger (compare the graph for $\mu = 0.8$ with that for $\mu = 0.5$). Figure 18b shows the avalanche half-length plotted against the artificial viscosity, μ, for the dimensionless time $t = 15$ and when $N = 40$ and $\Delta t = 0.02$ were chosen; the results obtained this way are connected by a solid curve. Those obtained with other cell numbers and time steps are also indicated by open squares and open circles (compare figure caption for details). As can be seen for $0.15 \leqslant \mu \leqslant 0.5$ the avalanche lengths differ only by less than 2% from each other despite the significant variation in μ. In the course of time, deviations can be larger, but we have in this example never experienced larger deviations than 5%.

To better be able to judge the influence of the artificial viscosity, let us denote the bracketed term on the right-hand side of equation (5.6) by Υ_j^n and compare it with the added numerical diffusive term ψ_j^n given in (5.11). Table 11 lists the values of the ratio ψ_j^n / Υ_j^n at the cell boundaries for a computation with 40 cells and a relatively

Table 11. *Computed values of the ratio* ψ_j^n/Υ_j^n *at the cell boundaries* $j = 1, 2, \ldots, n-1$ *for two values of the dimensionless time*

(Illustrates the influence of the artificial numerical diffusion on the numerical results of the lagrangian finite difference scheme, $t = 3$ shows 'normal' conditions, and $t = 6.08$ conditions for which the numerical diffusion is very large at places.)

$t = 6.08$		$t = 3$	
ψ_j^n/Υ_j^n	j	ψ_j^n/Υ_j^n	j
−0.662	1	−0.0182	1
−0.578393	2	0.0208271	2
−0.0182582	3	0.0195475	3
−0.0276056	4	0.00178509	4
−0.0207189	5	−0.0118564	5
−0.0109589	6	−0.0170913	6
−0.00585586	7	−0.0182387	7
−0.0044207	8	−0.0189614	8
−0.00229458	9	−0.0201346	9
0.00803963	10	−0.0207088	10
0.0378617	11	−0.0190769	11
0.0995491	12	−0.0147776	12
0.210721	13	−0.00559545	13
0.476799	14	0.0336206	14
3.40087	15	−0.00637224	15
−1.06669	16	−0.0196806	16
−0.265185	17	−0.0539494	17
0.141701	18	0.0063176	18
−0.683105	19	0.00543562	19
−0.536	1	−0.018	1
−0.321639	2	0.021001	2
−0.00874201	3	0.0196355	3
−0.0220201	4	0.00195338	4
−0.0185513	5	−0.0117513	5
−0.0106988	6	−0.0170883	6
−0.0062605	7	−0.01825	7
−0.00483781	8	−0.0189462	8
−0.00267503	9	−0.0201347	9
0.00702042	10	−0.020803	10
0.0342151	11	−0.0192835	11
0.0886563	12	−0.0149031	12
0.181925	13	−0.00460504	13
0.384331	14	0.0304324	14
1.58869	15	−0.00597336	15
−1.89262	16	−0.0197151	16
−0.356832	17	−0.00122947	17
0.14178	18	−0.0231558	18
0.221451	19	−0.0124601	19

large value of $\mu = 0.5$ at two times $t = 6.08$ and $t = 3$. At $t = 6.08$ the values of this ratio turned out to be unusually large, the case $t = 3$ corresponds more to regular conditions. As can be seen, the influence of the numerical diffusion is less than 3% under regular conditions and becomes only dominant with $\psi_j^n/\Upsilon_j^n > 1$ at a few grid points when $t = 6.08$. The frequency of occurrence of these unusual values of the numerical diffusive term has been very small in this case and was found to be well below 10% in a few other cases.

We have also varied the cell number (see figure 18*a*) and the step size and sampled the sensitivity for other values of ϕ, δ, ζ_0 and ϵ. It was found thereby that the selection of the numerical diffusivity is by far the most important parameter in the stabilization of the numerical scheme. To summarize, we thus performed all numerical comparisons with experiments with a cell number of $N = 40$ and a step size of $\Delta t = 0.02$ and selected a numerical value for μ in the interval $(0.2, 0.5)$.

Finally, it should also be indicated how it was decided when the granular avalanche came to rest. In general, each cell changes its velocity from being positive to being negative at its own time. If computations are arbitrarily continued then the cell velocities oscillate rather uncoordinatedly with decaying amplitudes. This oscillation is spurious and certainly unphysical. Based on this, one could determine the time when the avalanche comes to rest as that time when the last cell changes the sign of its velocity for the first time. After some experimentation it was found, however, that the termination of the computation and thus the fixing of the travel time of the granular avalanche was favourably chosen when at least half of the cells had changed the sign of their velocity. This criterion was maintained for all computations.

5.2. *Determination of similarity solutions*

Similarity solutions are obtained by solving the system of ordinary differential equations (2.12) subject to the initial conditions (2.13). We employed the Runge–Kutta method of order four, of which the convergence is $O(\Delta t^4)$, where Δt is the step size. This integration method is routine and had been tested before by Savage & Nohguchi (1988), so our presentation will be brief. We made a sensitivity study of the results (primarily by looking at the spreading of the parabolic pile, $g(t)$) to the choice of the step size and found that a step size of $\Delta t = 0.1$ was sufficient for an error of the spreading rate of less than 0.1 %, except when the avalanche was in a phase of strong deceleration. We thus chose $\Delta t = 0.1$ under 'regular' conditions and $\Delta t = 0.02$ when the centre of mass velocity $u_0(t)$ was smaller than 0.1. With this choice we were able to accurately reproduce the results presented by Savage & Nohguchi (1988).

5.3. *The validity of the schemes*

Obviously, integration of either of the schemes is only meaningful as long as

$$\delta_0 < \phi, \tag{5.12}$$

for otherwise the earth pressure coefficient, K_{actpass}, becomes complex valued. Similarly, we must have $\epsilon \leqslant 1$; $\lambda \leqslant O(\epsilon^{\frac{1}{2}})$ (lagrangian scheme); and $\lambda \leqslant O(\epsilon)$ (similarity solution). Thus the similarity solution is restricted both by the geometry of the pile (parabola) as well as the smallness of the curvature of the bed.

The other assumption of the similarity solution, not imposed by the general model, is the fact that the velocity can nowhere be uphill. This restricts the allowable aspect ratio to values satisfying the inequality (see Savage & Nohguchi 1988)

$$\frac{(2\epsilon K_{\text{actpass}} - a\zeta_0)\cos\zeta_0}{(\sin\zeta_0 - \tan\delta\cos\zeta_0)} \leqslant 1. \tag{5.13}$$

The maximum values of ϵ that satisfy this inequality depend on ζ_0, ϕ and δ. They will be denoted by ϵ_m and will be indicated where needed.

In the following we shall refer to the system of equations (2.10) and (2.11) as the general model (GM) and to the equations (2.12) and (2.13) and its solutions as the similarity model (SM).

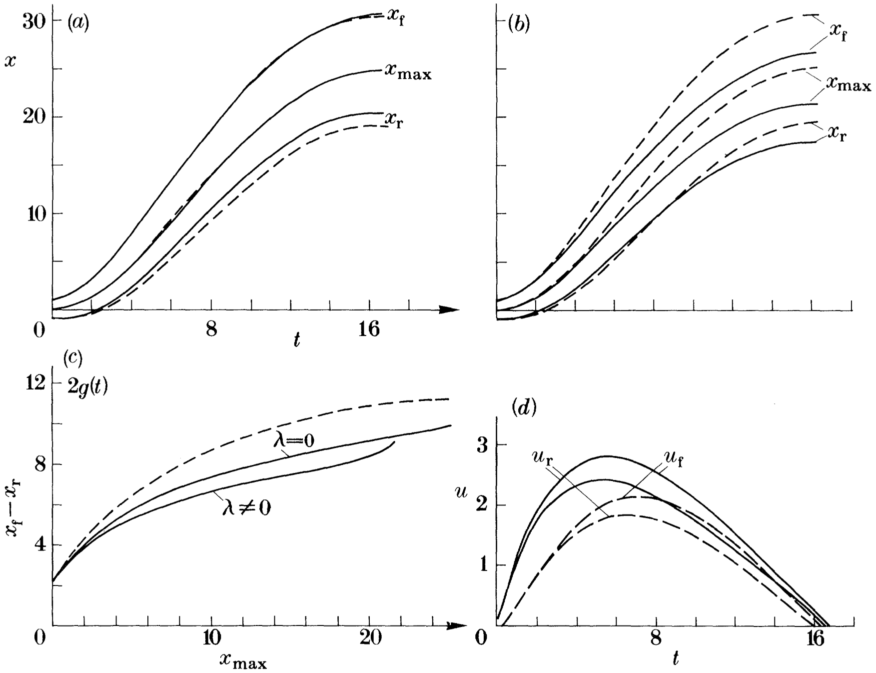

Figure 19. Numerical results obtained for the general model (GM) with/without the inclusion of the explicit curvature dependent term and for the similarity model (SM) without the explicit curvature-dependent term for a granular avalanche having initially the prabolic shape starting from rest on an exponential chute. Aspect ratio, $\epsilon = 0.5$; friction angles, $\phi = 37°$, $\delta_0 = 22°$; $k_{\text{wall}} = 0°$; chute parameters, $\zeta_0 = 22°$, $a = 0.1$. Initial conditions for SM: $x_0 = 0$; $u_0 = 0$; $g_0 = 1$; $g_0' = 0$. (*a*) Dimensionless x_r, x_{max}, x_f plotted against dimensionless time for GM with $\lambda = 0$ (full line) and for SM (dashed line). (*b*) As in (*a*) but for GM with $\lambda \neq 0$ (full line) and for SM (dashed line). (*c*) Avalanche length plotted against x_{max} for GM (full line) (with $\lambda = 0$ and $\lambda \neq 0$) and for SM (dashed line). (*d*) Front and rear end velocities u_f and u_r, respectively, for GM when $\lambda = 0$ (full line) and $\lambda \neq 0$ (dashed line).

To compare the computational results as obtained for the two models, an avalanche with an initial shape of a parabola of dimensionless length 2 and height 1 ($\epsilon = 0.5$) was chosen with $\phi = 37°$ and $\delta_0 = 22°$ and started from rest on an exponential bed with initial inclination angle $\zeta_0 = 60°$ and $a = 0.1$ (see equation (3.1)). The maximum aspect ratio for which the similarity solution holds for all time is in this case $\epsilon_m \approx 0.8$. The positions x_f, x_r and x_{max} of the granular pile were computed as functions of time for SM as well as for GM by omitting and including the explicit curvature term (here we mean the term containing λ in equation (2.11)). Results are shown in figure 19. Graph (*a*) compares the SM-solution with the GM-solution when $\lambda = 0$. Evidently the front positions, x_f, and the positions where the maximum depth arise, x_{max} agree very well; however, the positions of the rear end, x_r, deviate more and more from each other. For GM the pile becomes more and more asymmetrical as time proceeds. Graph (*b*) compares the two solutions when $\lambda \neq 0$. Here all positions x_f, x_r and x_{max} of the GM and SM solutions deviate from each other. The model avalanche of the SM travels farther than that of GM, the reason obviously being the enhancement of the basal Coulomb-type friction due to the additional contribution of the centrifugal term $\lambda\kappa\bar{u}^2$. Graph (*c*) displays the length of the avalanche in the three cases plotted against $x_{\max}$, and graph (*d*) illustrates how the leading edge and the trailing edge velocities as obtained for GM vary with time. Length and velocities depend conspicuously on $\lambda\kappa\bar{u}^2$ as they vary with time. The reason for this strong curvature dependence is that the product $\lambda\kappa\bar{u}^2$ is large even though $\lambda\kappa$ may be small along the entire track of the granular avalanche. This behaviour can easily be checked by starting with smaller initial slopes, ζ_0.

6. Comparison of theoretical results with experiments

6.1. *Implementation of bed friction properties and initial conditions for numerical computations*

6.1.1. *Bed friction angle*

Experiments have shown that the effective bed friction angle has a contribution due to wall friction and depends linearly on the depth of the granular pile:

$$\delta = \delta_0 + \epsilon k_{\mathrm{wall}}\, h, \tag{4.1}$$

or, equivalently and approximately

$$\tan\delta = \tan\delta_0 + \epsilon k_{\mathrm{wall}}\, h.$$

It was also demonstrated that under certain conditions when the bed was worn out by the large number of experiments, δ_0 showed a non-negligible variation along the bed. For the bed linings Makrolon and drawing-paper these dependencies are shown in figure 14. The dashed line in panel (*a*) of this figure is a parabolic eye-fitting to the data for the granular material quartz 0 on a Makrolon lining satisfying the functional form

$$\delta_0(x) = \begin{cases} -0.046(x-9)^2+29, & x < 18, \\ 25 & x \geqslant 18. \end{cases} \tag{6.1}$$

In computations for the GM, this formula (or equivalent ones) will be used in conjunction with (4.1) in every cell. Should in a cell the thus computed value of the effective bed friction angle exceed the internal angle of friction then it will be reduced to the value 0.999ϕ.

This procedure is not possible for the SM, because the bed friction angle in the similarity solution must have a constant value. To still find the 'best' value for δ in this case, the following procedure is suggested. Let $\tau(x,t)$ be the dimensionless basal shear stress. Then the total shear force acting at the bed of the parabolic pile is given by

$$\begin{aligned}\int_{x_{\mathrm{r}}}^{x_{\mathrm{f}}} \tau(x)\,\mathrm{d}x &= \int_{x_{\mathrm{r}}}^{x_{\mathrm{f}}} (\tan\delta_0 + \epsilon k_{\mathrm{wall}} H(x))\, H(x)\,\mathrm{d}x \\ &= \tan\delta_0 \int_{x_{\mathrm{r}}}^{x_{\mathrm{f}}} H(x)\,\mathrm{d}x + \epsilon k_{\mathrm{wall}} \int_{x_{\mathrm{r}}}^{x_{\mathrm{f}}} H^2(x)\,\mathrm{d}x \\ &= (\tan\delta_0 + \epsilon k_{\mathrm{wall}} \bar{H}) \int_{x_{\mathrm{r}}}^{x_{\mathrm{f}}} H(x)\,\mathrm{d}x, \end{aligned} \tag{6.2}$$

in which δ_0 and $\epsilon k_{\mathrm{wall}}$ are assumed to be constant and $\bar{H}$ is given by

$$\bar{H} = \int_{x_{\mathrm{r}}}^{x_{\mathrm{f}}} H(x)^2\,\mathrm{d}x \bigg/ \int_{x_{\mathrm{r}}}^{x_{\mathrm{f}}} H(x)\,\mathrm{d}x. \tag{6.3}$$

Equation (6.2) allows the following interpretation. The total shear force acting on the base of the parabolic granular pile is proportional to the total overburden pressure with a global Coulomb-type effective friction angle:

$$\tan\delta = \tan\delta_0 + \epsilon k_{\text{wall}} \bar{H}. \tag{6.4}$$

$\bar{H}$ can easily be calculated for a parabola with initial semi-length $g(0) = 2$ and height $h(0) = 1$ ($\epsilon = 0.5$), the result being

$$\bar{H} = 4/(5g(t)). \tag{6.5}$$

Consequently, we shall use for the construction of the similarity solutions the effective bed friction angle given by (6.4) and (6.5). Even though δ_0 was assumed to be constant in the above construction we shall assume δ_0 to depend on x_0, the position of the centre of gravity of the parabolic pile, where needed (for instance when analysing experiment 37 formula (6.1) will be used). We are aware that such a procedure is not consistent, but it is an acceptable compromise for weak dependencies of δ on x_0.

6.1.2. *Choice of initial depth profile*

Before release, the gate retaining the granular material was positioned vertically and the material behind the gate was nearly in the shape of a triangle, see figure 6*b*. Because initial profiles in the SM must be parabolic, adjustment has always been difficult in these cases. Appropriate initial conditions are also somewhat uncertain for the GM. We shall analyse the sensitivity of solutions to various choices.

A first difficulty consists in the selection of appropriate values of ϵ. It has been shown by Koch (1989) that equation (2.12) of the SM is insensitive to the chosen aspect ratio, ϵ, if the basal semi-length $g(0) = d$ is accordingly adjusted. A similar remark holds for the equations of GM. (Notice that for the derivation of the reduced equations the value of ϵ was important. But now that they are known we have the freedom to choose the scales as we please.) For a parabolic cap with width, b, volume, V, and semi-length, L, one has

$$\epsilon = 3V/4bL^2. \tag{6.6}$$

For our chute $b = 100$ mm, and experiments were performed with densest packings of particle piles having $V = 3, 2.25, 1.5$ l. With $L = 150$ mm this yields $\epsilon = 0.75, 0.5$, respectively. One possible set of initial conditions for the SM is therefore equation (2.12) with the specifications

$$X = Y = x_0 = u_0 = 0, \quad g(0) = 1, \quad f(0) = 0, \tag{6.7}$$

referred to as code 1 conditions. The effective aspect ratio in this case is 1.

It could not be guaranteed that the fillings of the granular material behind the confining plate had densest packing and that their volume was exactly as stated above. Table 5 suggested that some dilation must have occurred during motion. In code 2 we thus measured x_{r} and x_{f} from the photographs showing the triangular shape of the granular mass before its motion and chose as initial conditions

$$X = Y = 0, \quad x_0 = \tfrac{1}{2}(x_{\text{r}} + x_{\text{f}}), \quad u_0 = 0, \quad f(0) = 0, \quad g(0) = x_{\text{f}} - x_0, \tag{6.8}$$

referred to as code 2 conditions. For experiments 66 and 73 this resulted in $g(0) = 1.25$, corresponding to an effective aspect ratio of 0.8.

A still further and equally justified choice would be to determine the initial

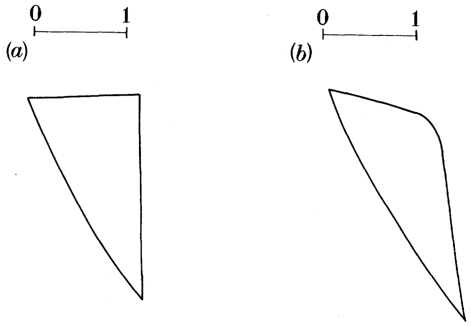

Figure 20. Initial geometry of the granular avalanche as taken from photographs for experiment 73; (*a*) code 5 and (*b*) code 6 conditions. In (*a*), enclosed volume, $V = 3.48$ l, $x_r = -1.55$, $x_f = 1$, $t = 0$; in (*b*), $V = 3.45$ l, $x_r = -1.27$, $x_f = 1.75$, $t = 0.9$.

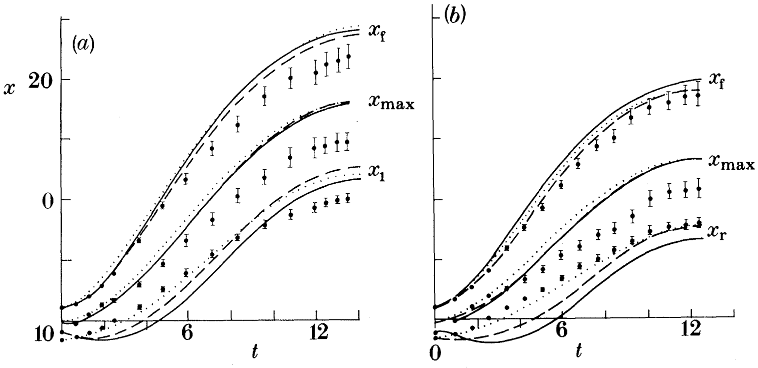

Figure 21. Experimental measurements and theoretical predictions of the positions x_f (leading edge), x_r (trailing edge) and x_{max} (position of maximum height) of the granular pile as functions of dimensionless time, t, for (*a*) experiment 66 and (*b*) experiment 73. Data points are shown with error bars. Theoretical curves were obtained using the SM with initial conditions: ——, code 1; – – –, code 2; …, code 3. (*a*) $\zeta_0 = 60°$, $a = 0.1$, $\epsilon = 1$, $\delta_0 = 26°$, $\phi = 33°$, $k_{wall} = 11°$ and $\epsilon_{max} = 0.373$, $t_m = 2.13$ (code 1), $\epsilon_{max} = 0.459$, $t_m = 1.0$ (code 2), $\epsilon_{max} = 0.532$, $t_m = 1.3$ (code 3). (*b*) $\zeta_0 = 60°$, $a = 0.1$, $\epsilon = 1$, $\delta_0 = 29°$, $\phi = 40°$, $k_{wall} = 12°$ and $\epsilon_{max} = 0.276$, $t_m = 2.75$ (code 1), $\epsilon_{max} = 0.338$, $t_m = 1.75$ (code 2), $\epsilon_{max} = 0.397$, $t_m = 0.9$ (code 3).

conditions from the first photograph for which the granular mass is already under motion. For the SM this yields the code 3 initial conditions

$$\left.\begin{aligned} t = t_0, \quad x_0 = \tfrac{1}{2}(x_f + x_r), \quad u_0 = \tfrac{1}{2}(u_r + u_f),\\ g(t_0) = x_f - x_0, \quad f(t_0) = g'(t_0), \end{aligned}\right\} \tag{6.9}$$

in which $g'(t_0) = \mathrm{d}g/\mathrm{d}t(t = t_0)$ has been determined from a plot of $(x_f - x_r)$ against t. For the GM we have also chosen the following three different initial (stationary) depth profiles.

1. Code 4 agrees with code 1, i.e., the initial triangular shape is replaced by a parabola at rest.
2. In code 5 the true triangular geometry is read from the photograph before any motion. For experiment 73 this is shown in figure 20*a*, the effective volume and aspect ratio being $V = 3.48$ and $\epsilon = 0.46$. The corresponding velocities are chosen to be zero.

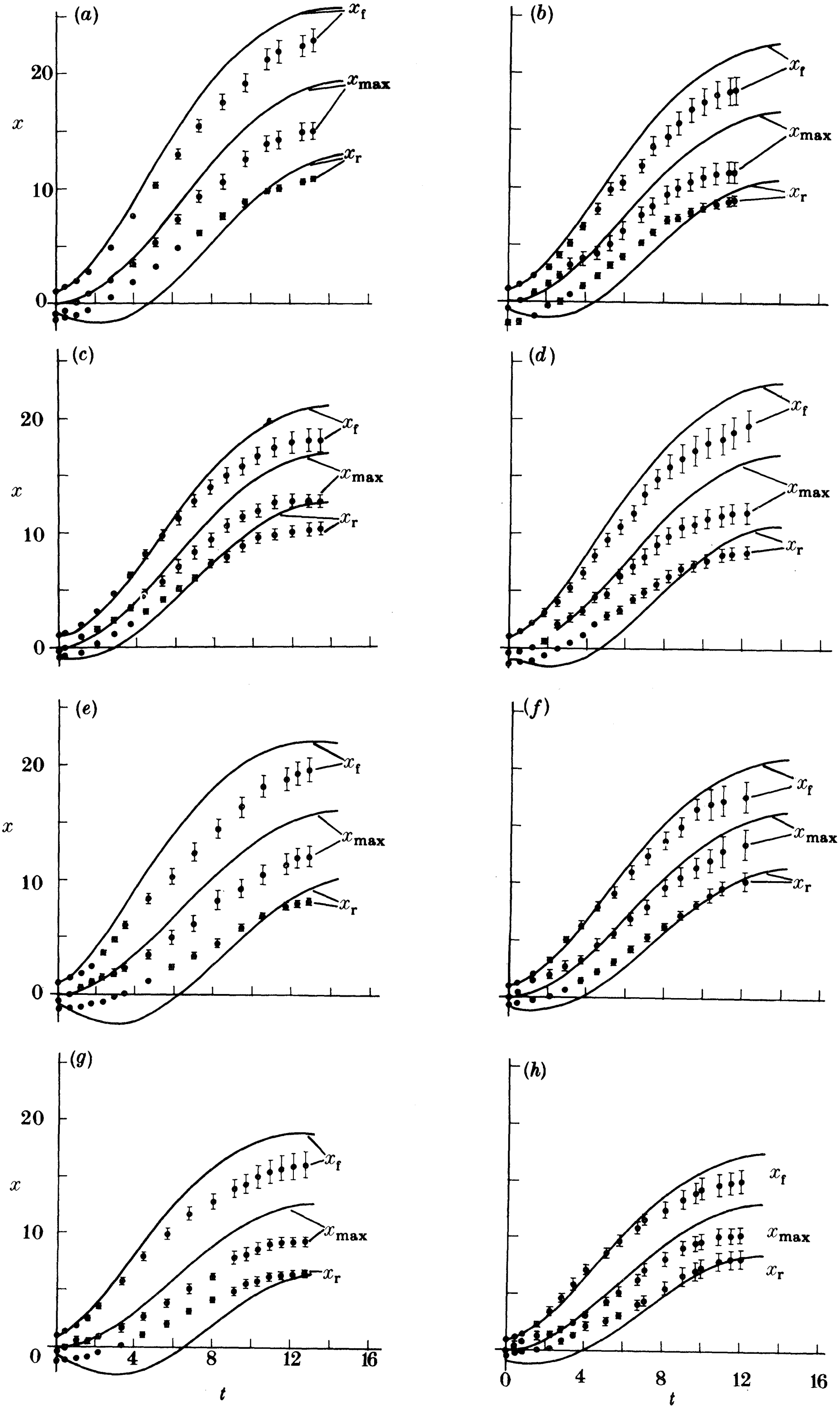

Figure 22. For description see opposite.

3. In code 6 the initial geometry was determined from a photograph for which the granular avalanche was already moving. The pile depth was read in these cases at 10 to 15 positions and a polynomial interpolation was used to construct the computational initial profile. For the second photograph of experiment 73 this fit is shown in figure 20*b*. The corresponding initial volume is $V = 3.452$ and the effective aspect ratio 0.32. The initial time was also determined from the photograph and the initial streamwise velocity was linearly interpolated between u_r and u_f, the initial velocities at the rear and front ends, respectively.

6.2. *Numerical results for the similarity model and comparisons*

Figure 21 compares experimental measurements and theoretical predictions of the evolution of the leading and trailing edge positions x_f, x_r as well as the position, x_{max}, where the maximum height of the granular avalanches occur for experiments 66 (3 l of Vestolen particles on a basal bed lined with drawing-paper) and 73 (3 l of quartz 0 particles on a basal bed lined with drawing-paper). The data points are shown with error bars and the curves represent the similarity solutions with codes 1, 2, and 3 initial conditions. No wall friction effects were taken into account.

It was stated in §5, equation (5.13) that the similarity solution is only meaningful when the effective aspect ratio is smaller than ϵ_m (given by the value obtained when the equality sign is used in (5.13)). The solutions of figure 21 do violate this condition at early times, because u_r is then negative. For each solution the transition time t_m when u_r changes sign is indicated in the caption together with the effective aspect ratio ϵ_{max} of the avalanche at that time.

The agreement between theory and experiment in figure 21 is rather poor, and depends upon the selected initial condition, of which the influence is particularly disappointing for x_r and code 1 and code 2 computations. The reason is obviously the occurrence of negative velocities u_r for small times because $\epsilon > \epsilon_m$. The better the inequality (5.13) is satisfied for early times (as, for example, for code 3 initial conditions) the better will the theoretical evolutions of x_r agree with observations. For experiments 66 and 73 the condition is violated at most at early times.

While the selection of the initial condition affects the prediction of the evolution of the rear end position, x_r, considerably, the corresponding effect on x_f and x_{max} is small. The prediction of x_{max} is generally poor, but this should be no surprise because for the parabolic profile $x_{max} = (x_f + x_r)/2$; that of x_r is an overshoot which is quite large for experiment 66. Further similar results for other experiments the details of which are described in the caption are shown in figure 22.

In summary it can be concluded that the SM solutions agree the better with experiments, the more the initial conditions fulfill the condition that $u_r(t_0) \geqslant 0$.

Figure 22. Experimental measurements and theoretical predictions using SM of x_r, x_f and x_{max} plotted as functions of dimensionless time, t, for experiments (*a*) 10, (*b*) 31, (*c*) 34, (*d*) 41, (*e*) 51, (*f*) 52, (*g*) 54, (*h*) 62 listed in table 12. All calculations were done with $a = 0.1$ and $\epsilon = 1$ and $\epsilon = 0.5$, respectively, depending on the amount of material. Data points show error bars and theoretical curves were obtained for code 1 initial conditions. The data points of experiments 31 and 41 are obtained from the video tapes, the resolution of which makes it impossible to determine the exact time the avalanche comes to rest. Also, for experiment 52 it was not possible to determine the total travel time. In those experiments this fact is assumed to be the cause for the early cessession of the motion. Except for later times when x_r is well predicted for experiments 52 and 62, all results are very poor and the differences between experiment and theory increase with time.

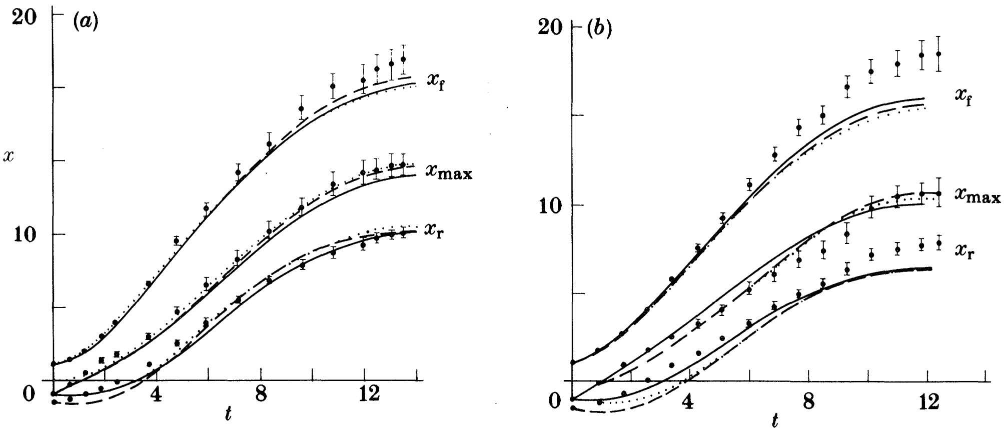

Figure 23. Experimental measurements and theoretical predictions of x_r, x_f and x_{max} as functions of dimensionless time for (*a*) experiment 66 and (*b*) experiment 73. Data points are the same as in figure 21. Theoretical curves obtained using the GM with initial conditions: ..., code 4; ---, code 5; ——, code 6. Computations have been performed for constant internal and bed friction angles, ϕ and δ, and wall friction effects being ignored. In (*a*), $\zeta_0 = 60°$, $a = 0.1$, $\epsilon = 1$, $\delta_0 = 26°$, $\phi = 37°$; in (*b*), $\zeta_0 = 60°$, $a = 0.1$, $\epsilon = 1$, $\delta_0 = 31.5°$, $\phi = 45°$.

Agreement of theoretical findings with observations is, however, poor in general. Thus the SM should only be used for diagnostic rather than prognostic purposes.

6.3. *Numerical results for the general model and comparisons*

6.3.1. *Bed friction angle only depth dependent*

Figure 23 illustrates the same comparison between experiments and theory as figure 21 but for the general model and for codes 4, 5 and 6 initial conditions. Agreement between experiment and observation is better than in the SM solutions, especially when the prediction of the temporal evolution of x_{max} is considered. Moreover, the positions x_r and x_f tend to be underpredicted (contrary to the SM solutions of figure 21). Negative velocities u_r at the rear end at early times do also occur, but they are consistent here, and differences in the initial conditions of codes 4, 5, and 6 are not very significant because differences in the positions x_r, x_f, x_{max} in the deposition zone are very small. Hence, all codes of the initial conditions are equivalent in the finite difference solution of GM, even though code 6 seems to be best.

In the foregoing comparisons, numerical values of the internal angle of friction, ϕ, and of the bed friction angle, δ, were used as measured and described in §4. These are static friction angles. Hungr & Morgenstern (1984*a*, *b*) found in their annular shear cell experiments that the dynamic internal friction angle was about 4° less than the angle of repose of the granular material as determined by us. Since the internal angle of friction, ϕ, of the glass beads is considerably smaller than for the other granular materials, we will choose the following reductions to obtain the dynamic internal friction angle: 3° for the glass beads and 4° to 5° for all other materials we used. As for the bed friction angle, δ, only a small reduction was made (0.5°–1.5°) such that the resulting angle would still lie within the variance band of the experiments.

Figure 24 shows the same comparison between experiments and theory as figure 23, the computations being done for code 6 initial conditions of the general model for experiments 66 and 73. Agreement in the prediction of the evolution of x_r, x_f and x_{max}

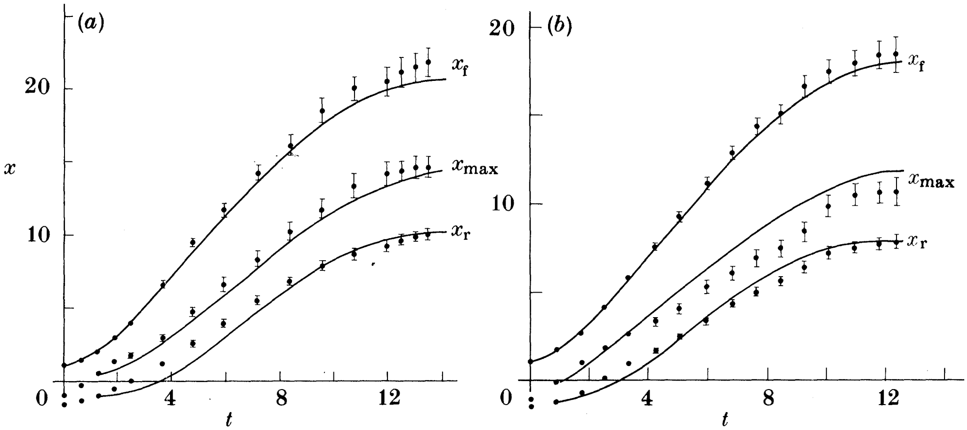

Figure 24. As figure 23 but the computations have been done with code 6 initial conditions using the GM equations, for (*a*) experiment 66 and (*b*) experiment 73. In comparison with figure 23, ϕ and δ have been reduced by 4° and 0.5° respectively in experiment 66, and 5° and 2.5° respectively in experiment 73. In (*a*), $\zeta_0 = 60°$, $a = 0.1$, $\epsilon = 1$, $\delta_0 = 26°$, $\phi = 33°$, $k_{wall} = 11°$. In (*b*), $\zeta_0 = 60°$, $a = 0.1$, $\epsilon = 1$, $\delta_0 = 29°$, $\phi = 40°$, $k_{wall} = 12°$.

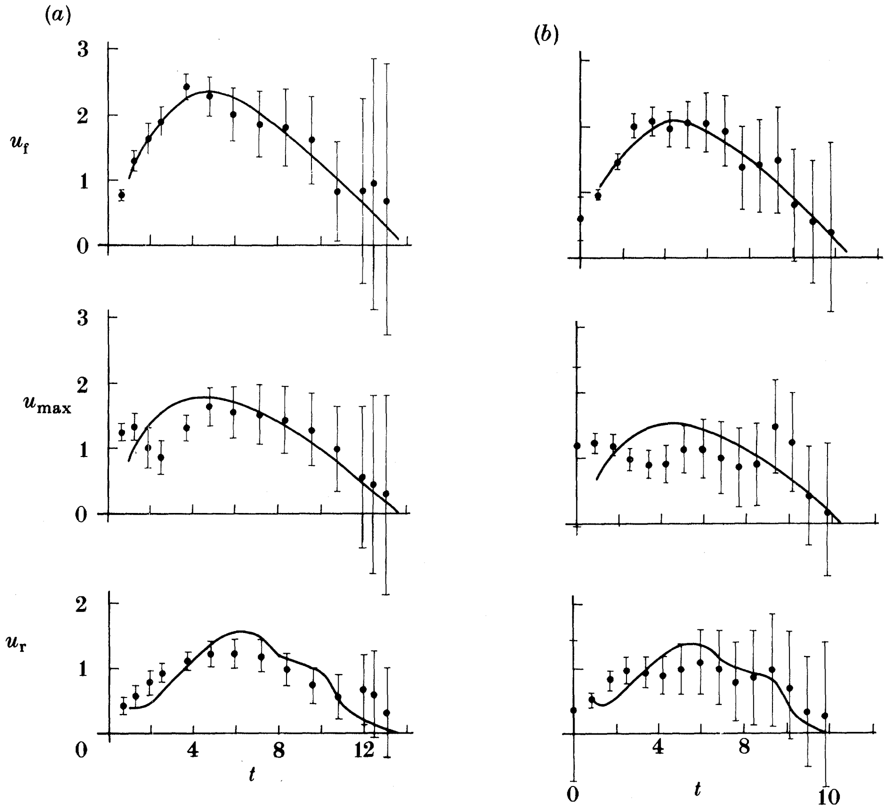

Figure 25. Evolution of the dimensionless velocities at the front u_f (top), at the position where the avalanche depth has a maximum u_{max} (middle) and at the trailing edge u_r (bottom) as deduced from experiment and theory under the same conditions as in figure 24. (*a*) Results for experiment 66, (*b*) for experiment 73.

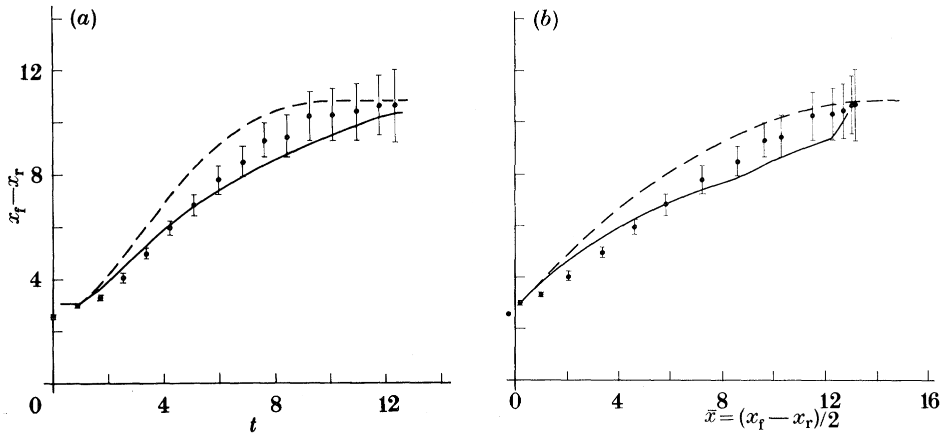

Figure 26. Evolution of dimensionless avalanche length plotted against dimensionless time and mean distance travelled as deduced from the photographs and obtained from computations for (*a*) experiment 73 and (*b*) experiment 66. Solid lines are obtained with code 6 initial conditions for the GM with parameters $\zeta_0 = 60°$, $a = 0.1$, $\epsilon = 1$, $\delta_0 = 29°$, $\phi = 44°$, $k_{\text{wall}} = 12°$. Dashed lines are obtained with code 6 initial conditions for the SM and code 3 initial conditions, with parameters $\zeta_0 = 60°$, $a = 0.1$, $\epsilon = 1$, $\delta_0 = 29°$, $\phi = 40°$, $k_{\text{wall}} = 12°$. (See also caption to figure 21.)

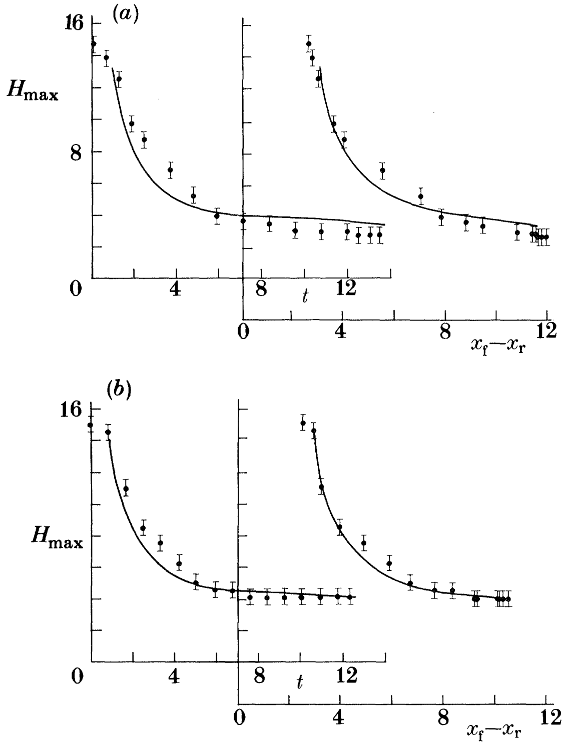

Figure 27. Experimental measurements and theoretical predictions of the maximum height plotted against dimensionless time and avalanche length, respectively, for (*a*) experiment 66, (*b*) experiment 73. The computations are for code 6 initial conditions of the GM. In (*a*), $\zeta_0 = 60°$, $a = 0.1$, $e = 1$, $\delta_0 = 26.5$, $\phi = 32°$, $k_{\text{wall}} = 11°$; in (*b*) $\zeta_0 = 60°$, $a = 0.1$, $\epsilon = 1$, $\delta_0 = 29°$, $\phi = 40°$, $k_{\text{wall}} = 12°$.

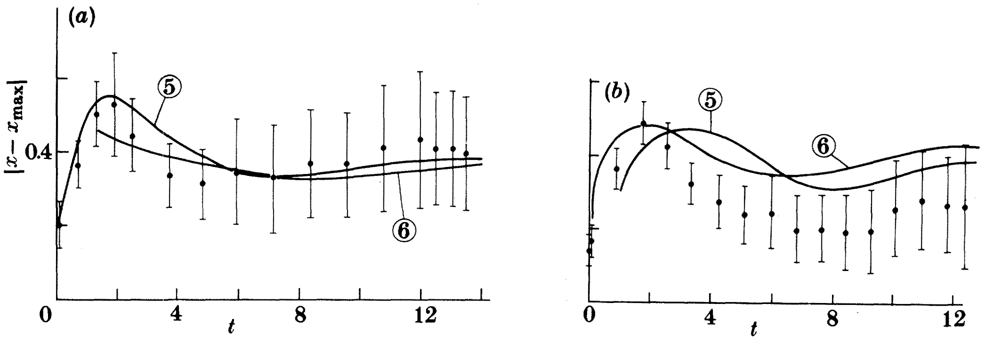

Figure 28. Experimental measurements and theoretical predictions of the relative position of the place where the maximum height occurs (as defined in equation (6.10)) plotted against dimensionless time (*a*) for experiment 66, (*b*) for experiment 73. The computations were done for code 5 and code 6 initial conditions of the general model. In (*a*), $\zeta_0 = 60°$, $a = 0.1$, $\epsilon = 1$, $\delta_0 = 26°$, $\phi = 33°$, $k_{\text{wall}} = 11°$; in (*b*), $\zeta_0 = 60°$, $a = 0.1$, $\epsilon = 1$, $\delta_0 = 29°$, $\phi = 44°$, $k_{\text{wall}} = 12°$.

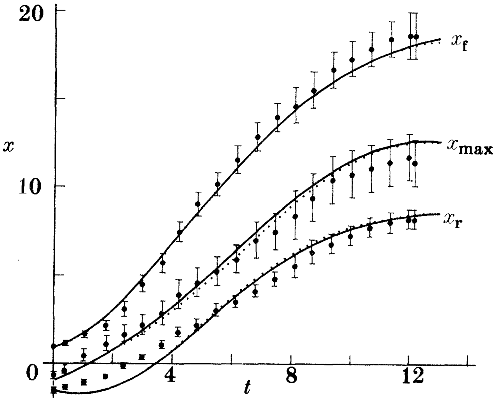

Figure 29. Experimental measurements and theoretical predictions (using GM) of x_{r}, x_{f} and $x_{\max}$ as functions of dimensionless time for experiment 37 (3 l of quartz 0 granules and a bed lining of Makolon). Computations were done by using the law (4.1) for the bed friction, once with a constant value $\delta_0 = 28°$ (dotted line) and once for a variable δ_0 (solid line) as given by equation (6.1). Differences in the results are small. Aspect ratio, $\epsilon = 1$; friction angles, $\phi = 41°$; $\delta_0 = 28°$; $k_{\text{wall}} = 12°$; chute parameters, $\zeta_0 = 60°$, $a = 0.1$.

between theory and observation is very good. Figure 25 compares the observed and computed non-dimensional velocities at the front, u_{f}, at the rear, u_{r}, and at the position where the height is a maximum, $u_{\max} = u(x_{\max})$. Agreement between theory and experiments for the velocities is slightly less convincing than for the positions mainly because the velocities inferred from the photographic prints are fraught with larger errors.

Comparisons of other variables as deduced from experiment and derived from theory are equally convincing for the two selected experiments. Figure 26 displays the evolution with time of the avalanche length and figure 27 shows that of the maximum height $h_{\max}$ within the granular pile for both experiments 66 and 73. An interesting variable is also the position where the maximum height arises relative to the position of the trailing edge and scaled with the actual length for the granular avalanche. Denoting this variable by $x_{\max}^{\text{rel}}$, it is defined by

$$x_{\max}^{\text{rel}} = (x_{\max} - x_{\mathrm{r}})/(x_{\mathrm{f}} - x_{\mathrm{r}}). \tag{6.10}$$

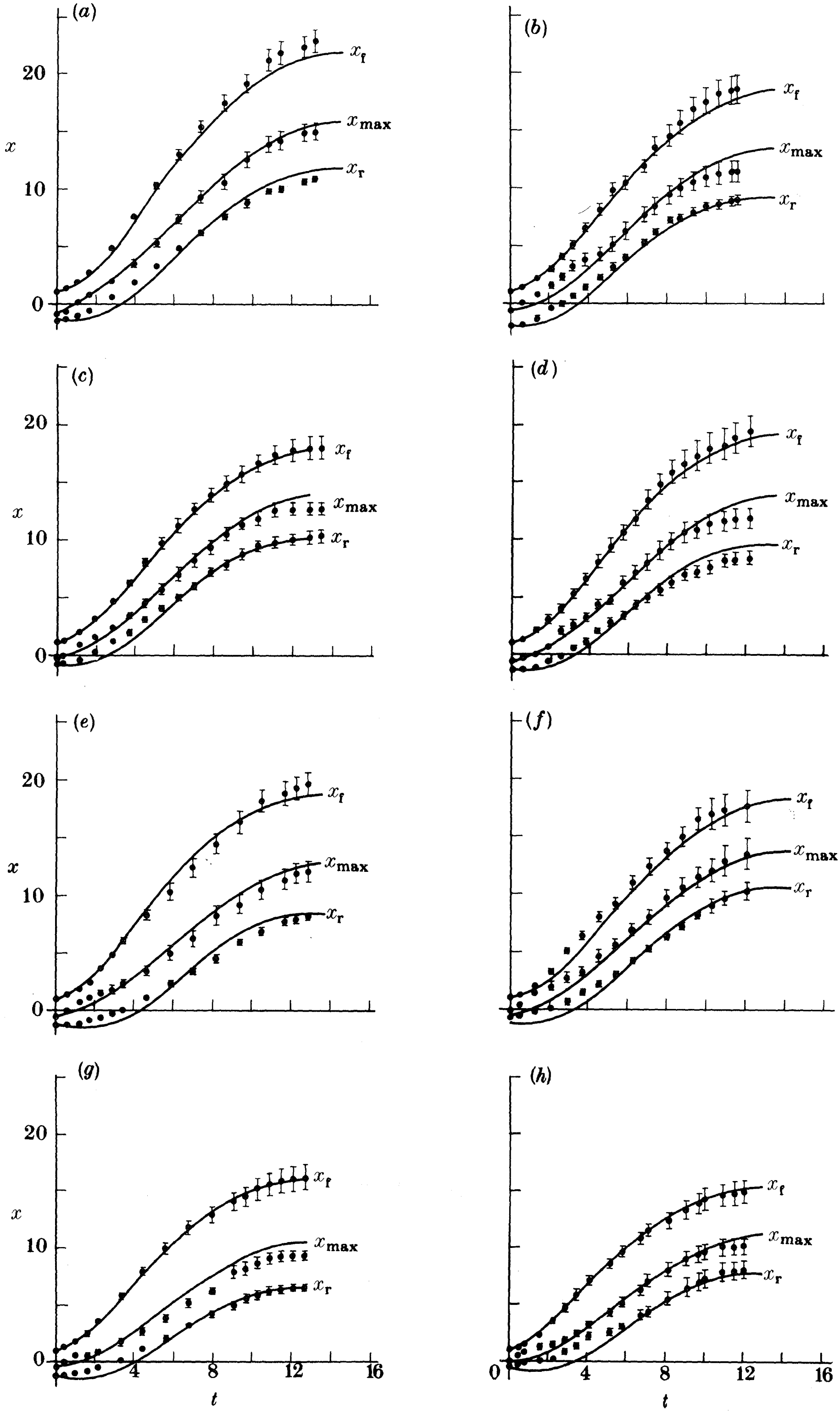

Figure 30. For description see opposite.

Values larger (smaller) than 0.5 indicate that the maximum height lies in the front (rear) part of the avalanche. We have determined this quantity for experiments 66 and 73 from the photographs and from computations of the GM using codes 5 and 6 initial conditions. Results are shown in figure 28. They indicate a surprising satisfactory agreement between theory and experiment both qualitatively and quantitatively.

6.3.2. *Bed friction angle position dependence*

It was mentioned before that repeated experiments wore down the bed and resulted in a position dependence of the bed friction angle (see figure 14*a*, *b* which summarize the findings for the bed lining Makrolon). For the material quartz 0 a curve fit to the measured bed friction angle $\delta_0(x)$ was given in equation (6.1); it was used in evaluations of the effective bed friction angle (subsection 4.1) and in computations and reproductions of experiment 37 (3 l of quartz 0 on bed-lining Makrolon). Figure 29 shows a comparison of experiment with computational predictions for x_r, x_f and $x_{\max}$ when code 6 initial conditions were used for both a variable δ_0 (according to equation (6.1)) and a constant $\delta_0 = 28°$. The computational results hardly differ from each other and agreement between theory and experiment is satisfactory. Thus consideration of the variability of the bed friction angle is not needed in this example.

6.3.3. *Additional results supporting the model*

The above comparison between observational results and theoretical predictions involved only three experiments. This is not sufficient to be able to claim adequacy of the theoretical model. We have performed many more comparisons and here we summarize the good results. Table 12 lists the experimental conditions for which satisfactory agreement has been obtained, and figure 30 shows a comparison between experimental findings and computational results. All computations were done with code 5 initial conditions. As seen from the table, good results are obtained when the bed friction angle, δ, is considerably smaller than the internal angle of friction. These GM comparisons are the same as those in figure 22, which were obtained with SM solutions. The better performance of the GM is very convincing.

6.3.4. *Limitation of the model*

Comparison of numerical solutions of the GM with experiments was not always successful in the sense that sufficient agreement would have been obtained. Table 13 lists four cases in which computational predictions were poor. Figure 31 presents a comparison between experiments and computational predictions for these four cases. In the computations, code 5 initial conditions were used. In panels (*a*) and (*b*) the

---

Figure 30. Experimental measurements and theoretical predictions (using GM) of x_r, x_f and $x_{\max}$ plotted as functions of dimensionless time, t, for experiments (*a*) 10, (*b*) 31, (*c*) 34, (*d*) 41, (*e*) 51, (*f*) 52, (*g*) 54, (*h*) 62, listed in table 12. For all calculations $a = 0.1$ and $\epsilon = 1$. Data points are shown with error bars and theoretical curves were obtained for code 5 initial conditions. All graphs demonstrate a satisfactory agreement between experiment and theory. The data points of experiments 31 and 41 are obtained from the video tapes, the resolution of which makes it impossible to determine the exact time the avalanche comes to rest. Also, for experiment 52 it was not possible to determine the total travel time. In those experiments this fact is assumed to be the cause for the early cessession of the motion. Except at early times for which x_r is not well predicted, the figures demonstrate a surprisingly accurate agreement between theory and experiments.

Table 12. *Experimental conditions for which agreement between theory and experiment was satisfactory*

experiment no.	granular material	bed material	volume/l	initial slope, ζ_0/deg	internal angle of friction/deg	bed friction angle, δ_0/deg	wall friction angle, k_{wall}/deg
10	Vestolen	Makrolon	3	60	32	25	10
51	Vestolen	drawing-paper	3	54	32	25.5	11
52	Vestolen	drawing-paper	1.5	54	32	25.5	11
34	quartz 0	drawing-paper	1.5	60	40	27.5	12
62	quartz 0	drawing-paper	1.5	54	40	29	11
54	quartz 0	drawing-paper	3	54	40	29	11
31	marmor 0	Makrolon	3	60	43	27	12.5
41	quartz 1	drawing-paper	3	60	39	27	11.5

Table 13. *Experimental conditions for which agreement between theory and experiment was poor*

experiment no.	granular material	bed lining	volume/l	ζ_0/deg
85	Vestolen	sandpaper	3.0	60
87	quartz 0	sandpaper	3.0	60
6	glass 0	Makrolon	1.5	60
83	glass 0	sandpaper	3.0	60

evolution of x_{f} and $x_{\max}$ is reasonably well predicted in the first half of the movement of the granular avalanches, that of x_{r} is generally slower than in the observations. At later times, deviations are bigger and, in particular, the computational avalanche comes to a halt considerably earlier than the granular avalanche in the experiment.

Scrutinizing all the experiments that were performed, it was recognized that travel times of granular avalanches on the bed-lining sandpaper were rather long, but that travel distances perhaps were not considerably larger than with other bed linings. In experiments 85 and 87 of figure 31, δ_0 and ϕ are close to each other, so that the total bed friction angle was often formally exceeding the internal angle of friction. In these circumstances we used $\delta = 0.999\phi$. With $\delta \approx \phi$, the basal surface is no longer dynamically different from any internal surface of the granular pile. We suspect, but have not been able to support this with an explicit proof, that the basal surface does no longer act as a clear and distinct sliding surface and that the velocity distribution is not as uniform over depth and has now a substantial shear layer. This problem clearly warrants further study.

A case which appears to be on the borderline is the avalanche of experiment 83, see figure 31*c*. Here the distance travelled by the theoretical avalanche is the same as that of the experimental avalanche when x_{f} and $x_{\max}$ are considered, but x_{r} is considerably larger for the experiments than the computations. The computational travel time is larger, and it appears that in the settling-down phase the model

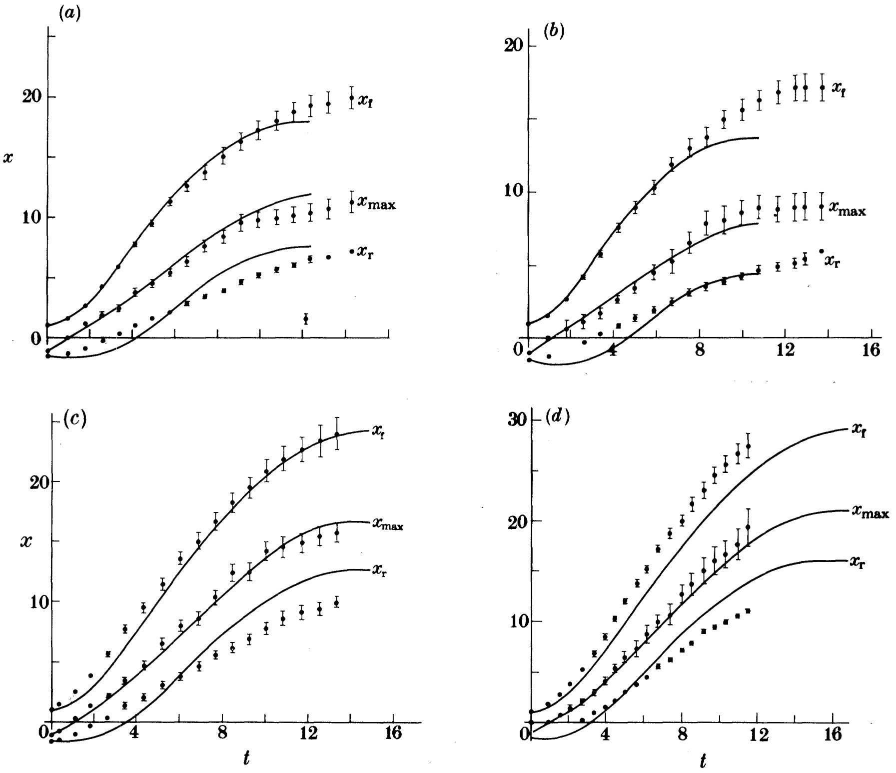

Figure 31. Experimental measurements and theoretical predictions of the positions x_f, x_r and x_{max} of four different granular avalanches plotted against dimensionless time for (*a*) experiment 85, (*b*) 87, (*c*) 83 and (*d*) 6. Data points show error bars, and theoretical curves were obtained for code 5 initial conditions. In (*a*), $\zeta_0 = 60°$, $a = 0.1$, $\epsilon = 1$, $\delta_0 = 33°$, $\phi = 33°$, $k_{wall} = 11°$; in (*b*) $\zeta_0 = 60°$, $a = 0.1$, $\epsilon = 1$, $\delta_0 = 37.5°$, $\phi = 40°$, $k_{wall} = 12°$; in (*c*) $\zeta_0 = 60°$, $a = 0.1$, $\epsilon = 1$, $\delta_0 = 24°$, $\phi = 28°$, $k_{wall} = 9°$; in (*d*) $\zeta_0 = 60°$, $a = 0.1$, $\epsilon = 1$, $\delta_0 = 20°$, $\phi = 28°$, $k_{wall} = 9°$. The experimental conditions for the four experiments are summarized in table 13.

avalanche decelerates much faster. In this case, $\delta_0 < \phi$ by 4° and the total bed friction angle, δ, came close to the value of ϕ but did not exceed it.

Finally, experiment 6 shows an extreme case for which the travel time of the theoretical avalanche is substantially bigger and the computed avalanche length much smaller than for the corresponding experimental avalanche. Here δ and ϕ differ by 8°; the reason for the failure of the theory is likely to differ from the previous one. We suspect that with decreasing total mass of the avalanche and when the coefficients of restitution are high then the particles are relatively free to move and prone to interact in collisions so that a considerable amount of energy is stored in the fluctuating motion. Alternatively, we are not able to rule out inaccuracies in observations when the total mass of the avalanche is small, which could also explain the inadequacy in experiment 6.

7. Concluding remarks

In this paper we have presented a comparison of results obtained with laboratory experiments on the motion of a finite mass of a cohesionless granular material down an exponentially curved bed with computational predictions obtained with the theoretical model of Savage & Hutter (1990). The analysis is based upon depth-averaged conservation of mass and linear momentum equations and the assumptions of material incompressibility, small depth-to-length ratio of the pile, small to moderate bed curvature, and simple Coulomb-like constitutive behaviour both for the interior of the granular material and for the bed friction. Experiments were performed with seven different granular materials and three different bed linings exhibiting a large range of material properties, expressed in the values for the internal friction angle, bed friction angle and coefficients of restitution. For the different granular materials and for the three bed linings these coefficients were experimentally determined. The motion of a finite mass (either 3, 2.25 or 1.5 l) of the granular materials from initiation to runout along the exponentially curved bed was photographed and video-recorded and from this information the temporal evolutions of the rear end, x_{r}, and the leading edge, x_{f}, and the position where the maximal depth of the avalanche arises were inferred, as were the velocities of these points and the maximum depth.

Numerical solutions for the evolution of the pile of granular material as it is released from rest, moves down the slope and eventually comes to rest on the flat portion of the exponentially curved bed were obtained by two different methods. In the lagrangian finite difference approximation, which was previously successfully used by Savage & Hutter (1989, 1990), the general evolution of the moving and deforming pile was followed from an initial profile, and shape and velocity distributions were determined through time. In the similarity model, the pile geometry was restricted to parabolic shape and the centre of mass velocities and the pile's semi-spread could be determined through time only provided the curvature of the bed was small. Initial conditions in the experiments were not as simply and clearly defined as one would desire; and in particular for the similarity model, initial pile geometries had to be transferred to parabolic shape for computations. For each of the models (GM and SM) three different initial conditions for the pile geometry and the velocity distribution were motivated and constructed and computational solutions for x_{r}, x_{f}, $x_{\max}$ and (in some cases) the respective velocities were determined. As for the various initial conditions that were employed, the results of the general model were relatively insensitive to them. This supports the general feeling that the evolutions of the granular piles are relatively insensitive to initial pile geometries. For the similarity solutions these initial conditions are more important, and in particular only a qualitatively correct prediction is possible if the aspect ratio of the pile is small. Comparison of the solutions with the experimental findings revealed the following results.

1. The theoretical model reproduces the evolution of the granular avalanche as it evolves from the laboratory experiments with good to satisfactory coincidence, provided the bed has a distinguishable sliding surface. In other words, when the internal angle of friction, ϕ, is larger than the bed friction angle, δ, then the granular mass will move essentially as a passively deforming body and the friction angles ϕ and δ only affect the earth pressure coefficient. The theory reproduces the experiments sufficiently well in this case.

2. When the bed friction angle, δ, and the internal angle of friction, ϕ, are close to each other, with $\delta \gtrsim \phi$, then the theory fails and to make it work we set $\delta = 0.999\phi$; in those cases the theory does not match experiments. Obviously, there is no clearly defined slip surface in this case; the material will yield at all depths in this case, so

that development of a distributed shear deformation through the pile depth is possible. If this interpretation is correct then our depth-averaged equations are inappropriate and deviation of theoretical predictions from experimental findings cannot be a surprise.

3. When the masses of the moving granular piles are very small such that the granules can bounce extensively within the pile, then the theory also seems to deviate from the experiments. In this case a large amount of energy must be stored in the fluctuating motion of the particles. The study of this behaviour also warrants further investigation.

4. The similarity solutions do not in general yield positions of the leading and the trailing edges which show sufficient agreement with experimental observations to be useable for prognostic purposes, but when curvature effects are small then the SM may be used for diagnostic analyses. In such circumstances $\delta = \alpha$, where α denotes the 'Pauschalgefälle'.

In short we may claim that the model equations of the GM presented by Savage & Hutter (1990) are appropriate ones if a cohesionless granular material obeying a Coulomb-type internal friction law is moving on a bed with a bed friction angle that is clearly smaller than the internal angle of friction.

The experimental work was performed at the Laboratory of the Institute of Mechanics, Technological Institute, Darmstadt, Germany. We thank the workshop and the laboratory personnel, in particular Mr Henrich, Mr Hofmann, Dr Leutloff and Mr Wall for their invaluable help. Mrs Danner typed the manuscript. The final drawings were done at the Laboratory of Hydraulics, Hydrology and Glaciology at ETH, Zürich; Mrs Wiederkehr is responsible for the artwork.

The final text, as well as part of the layout of the computations, were prepared while K.H. was a guest scientist at the Swiss Federal Institute of Snow and Avalanche Research, Weissfluhjoch Davos. K.H. thanks its Director, Professor C. Jaccard for the financial support and for the pleasant and stimulating surroundings that made this work possible. He also would like to express his thanks and appreciation for the many stimulating discussions with Dr H.-U. Gubler.

References

Anderson, D., Tannehill, J. & Pletcher, R. 1984 *Computational fluid mechanics and heat transfer.* New York and London: McGraw Hill.

Gubler, H.-U. 1987 Measurements and modelling of snow avalanche speeds. In *Avalanche formation, movement and effects*. IAHS Publ. no. 162 (ed. B. Salm & H.-U. Gubler), pp. 405–420.

Huber, A. 1980 Schwallwellen in Seen als Folge von Felsstürzen. *Mitteilung No. 47 der Versuchsanstalt für Wasserbau, Hydrologie und Glaziologie an der ETH*, pp. 1–122.

Hungr, O. & Morgenstern, N. R. 1984 *a* Experiments on the flow behaviour of granular materials at high velocity in an open channel flow. *Geotechnique* **34**, 405–413.

Hungr, O. & Morgenstern, N. R. 1984*b* High velocity ring shear tests on sand. *Geotechnique* **34**, 415–421.

Hutter, K. & Nohguchi, Y. 1990 Similarity solutions for a Voellmy model of snow avalanches with finite mass. *Acta mech.* (In the press.)

Hutter, K. & Savage, S. B. 1988 Avalanche dynamics: The motion of a finite mass of gravel down a mountain side. *Proceedings of the 5th International Symposium on Landslides, July 7–9, Lausanne, Switzerland.* 7 pp. Rotterdam and Brookfield: A. A. Balkema.

Hutter, K., Plüss, C. H. & Maeno, N. 1988 Some implications deduced from laboratory experiments on granular avalanches. *Mitteilung No. 94 der Versuchsanstalt für Wasserbau, Hydrologie und Glaziologie an der ETH*, pp. 323–344.

Hutter, K., Plüss, C. H. & Savage, S. B. 1990 Dynamics of avalanches of granular materials from initiation to runout. Part II: laboratory experiments. (In preparation.)

Koch, T. 1989 *Bewegung einer Granulatlawine entlang einer gekrümmten Bahn*. Diplomarbeit, Technische Hochschule Darmstadt, pp. 1–222.

Nohguchi, Y., Hutter, K. & Savage, S. B. 1989 Similarity solutions for a finite mass granular avalanche with variable friction. *Continuum Mech. Thermodyn.* **1**, 239–265.

Norem, H., Kristensen, K. & Tronstad, K. 1986 The Ryggfonn project. Avalanche data from the winter 1984/85. Norwegian Geotechnical Institute report 58120-8.

Norem, H., Kristensen, K. & Tronstad, K. 1988 The Ryggfonn project. Avalanche data from the winter 1987/88. Norwegian Geotechnical Institute report 58120-12.

Perla, I. P., Cheng, T. T. & McClung, D. M. 1980 A two-parameter model of snow avalanche motion. *J. Glaciology* **26** (94), 197–207.

Perla, R. & Martinelli, M. 1978 *Avalanche Handbook*. U.S. Department of Agriculture Forest Service, Agriculture Handbook, 489.

Plüss, C. H. 1987 *Experiments on granular avalanches*. Diplomarbeit, Abt. X, Eidg. Technische Hochschule, Zürich, pp. 1–113.

Roberts, A. W. 1969 An investigation of the gravity flow of noncohesive granular materials through discharge chutes. *Trans. Am. Soc. mech. Engrs.* **91**, 373–381.

Salm, B. 1968 On nonuniform steady flow of avalanching snow. IAHS Publ. No. 79, pp. 19–29. Bern: IUGG/IAHS General Assembly.

Savage, S. B. 1979 Gravity flow of cohesionless granular materials in chutes and channels. *J. Fluid Mech.* **92**, 53–96.

Savage, S. B. & Hutter, K. 1989 The motion of a finite mass of granular material down a rough incline. *J. Fluid Mech.* **199**, 177–215.

Savage, S. B. & Hutter, K. 1990 The dynamics of avalanches of granular materials from initiation to runout, Part I: Analysis. *Acta mech.* (In the press.)

Savage, S. B. & Nohguchi, Y. 1988 Similarity solutions for avalanches of granular materials down curved beds. *Acta Mech.* **75**, 153–174.

Voellmy, A. 1955 Über die Zerstörungskraft von Lawinen. *Schweizerische Bauzeitung* **73**, 159–162, 212–217, 246–249, 280–285.

Received 9 January 1990; accepted 23 May 1990

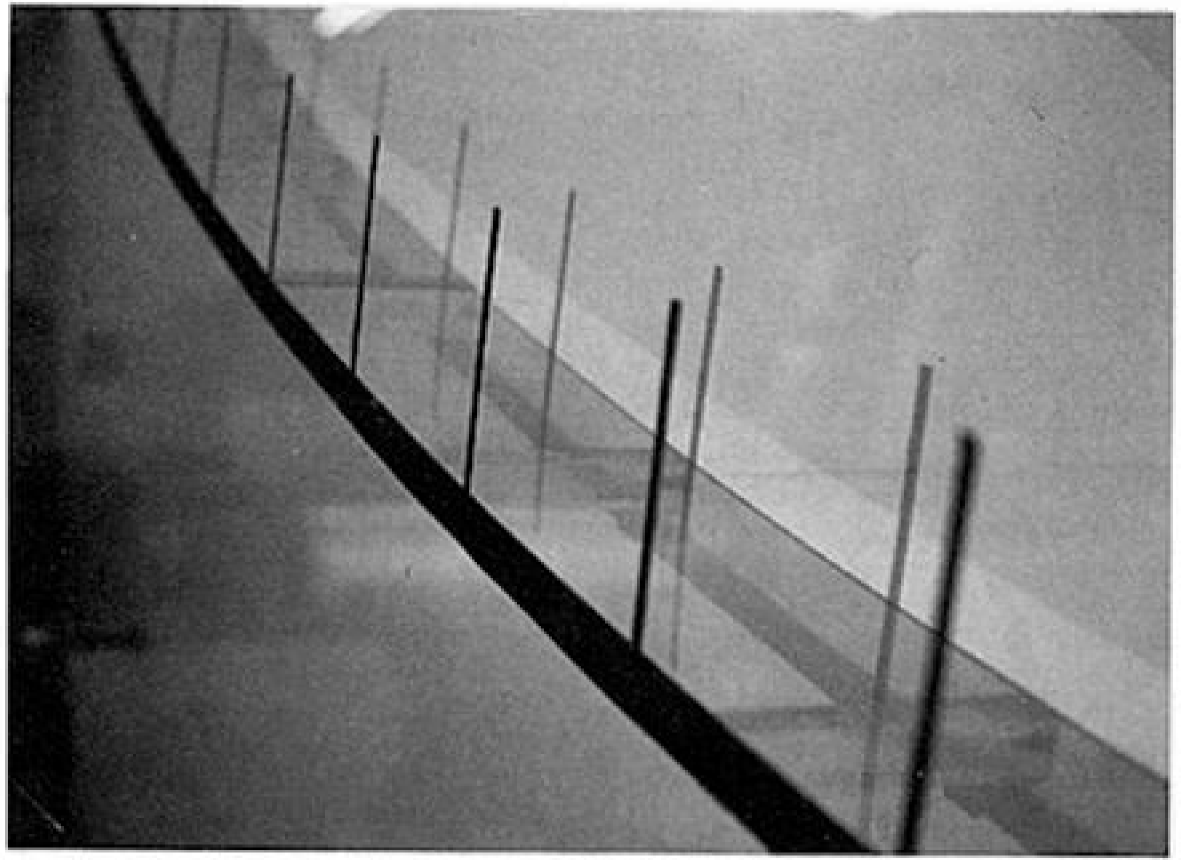

gure 5. Chute made of Makrolon (a kind of plexiglass, but softer). Visible on the front plexiglass wall is the distance scale.

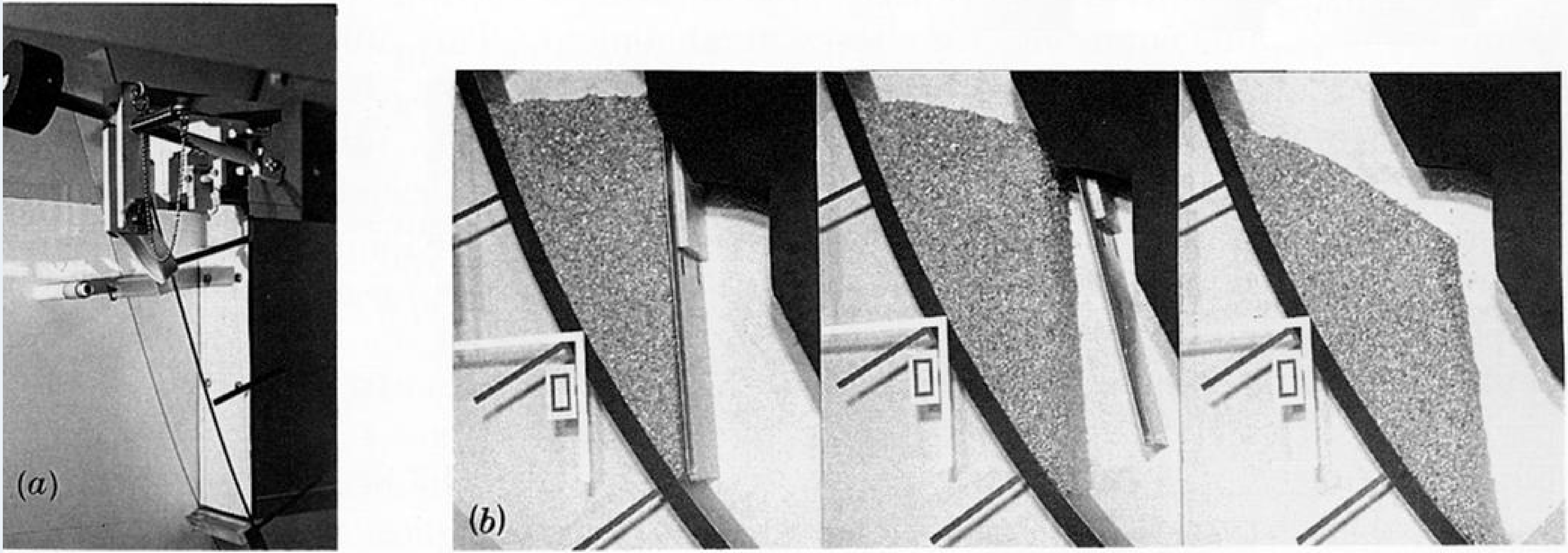

igure 6. (*a*) Detail A in figure 4 showing the vertical plate confining the granular material. By ulling the bolt, the plate rotates about a horizontal axle in the counter-clockwise direction. (*b*) The lease of 3 l of granular material in a chute having 60° initial slope angle. The nominal speed with hich the shots were taken was 15 frames per second.

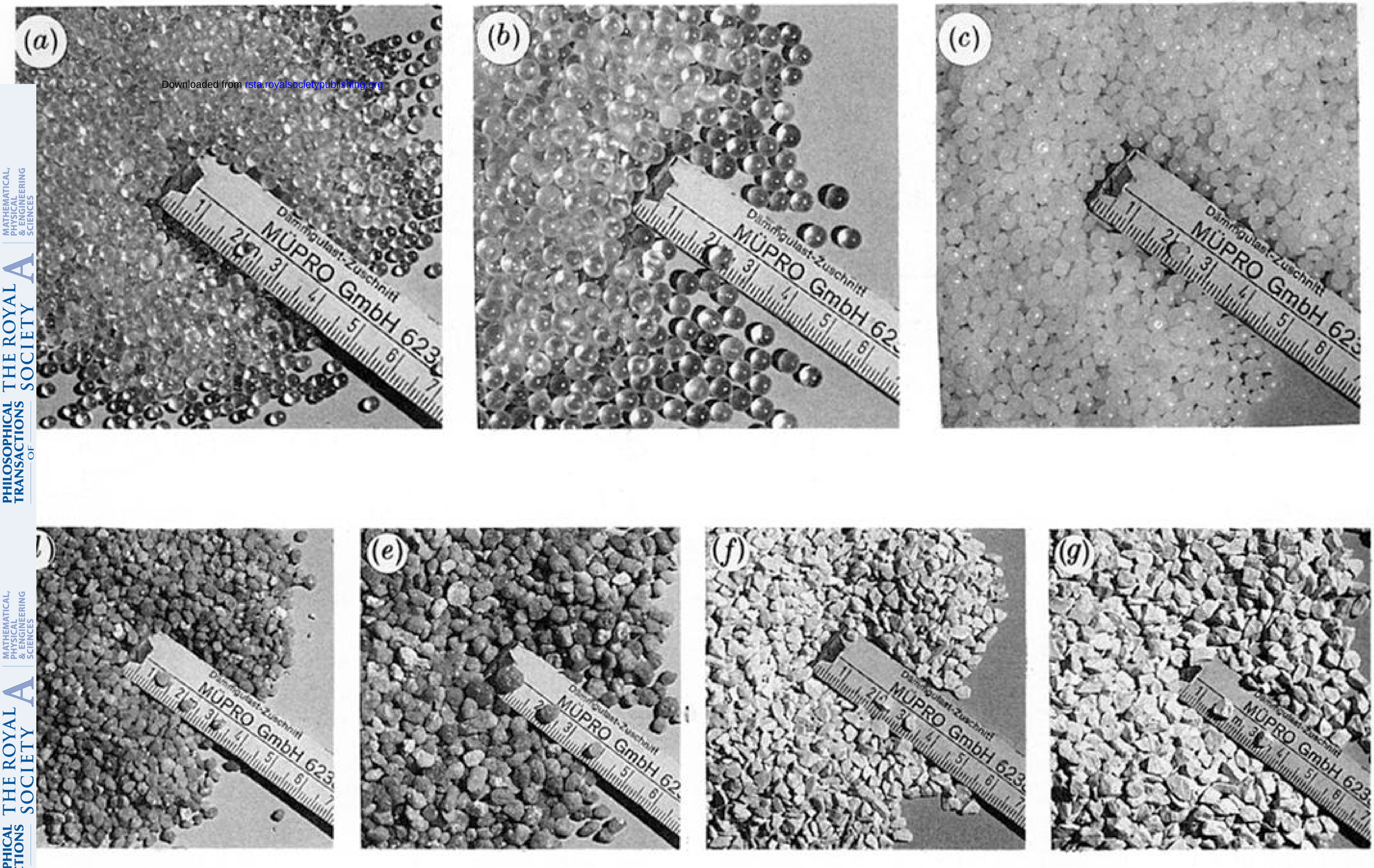

igure 7. Samples of the granular materials: (*a*) glass 0 (3 mm); (*b*) glass 1 (5 mm); (*c*) Vestolen; (*d*) quartz 0 (3 mm); (*e*) quartz 1 (5 mm); (*f*) marmor 0 (3 mm); (*g*) marmor 1 (5 mm).

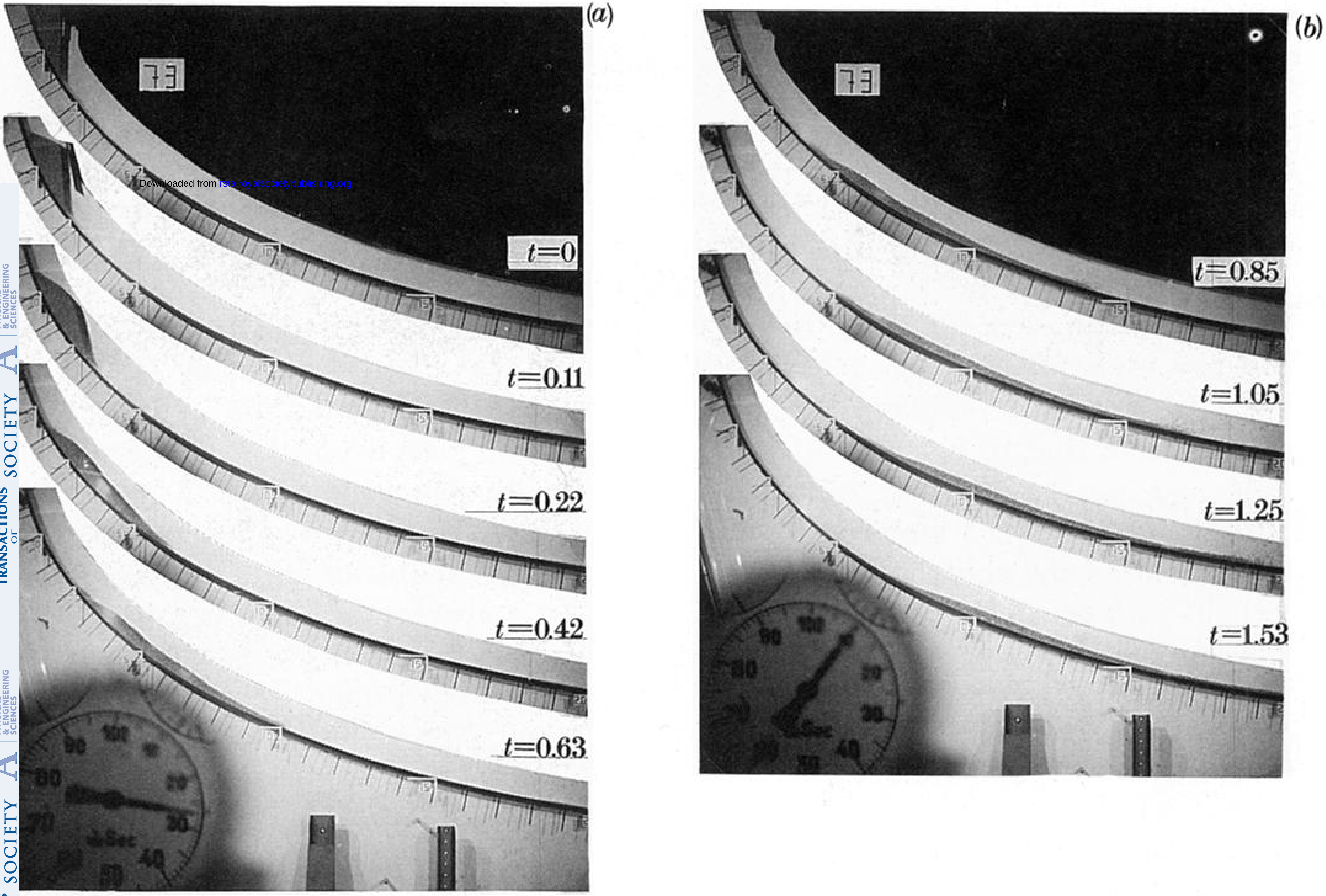

gure 8. Series of photographs (experiment 73) taken at different dimensionless times of a granular aterial (3 l of quartz 0 particles) moving down the exponentially curved chute, the bed of which roughened by drawing-paper and the initial slope angle is 60°.

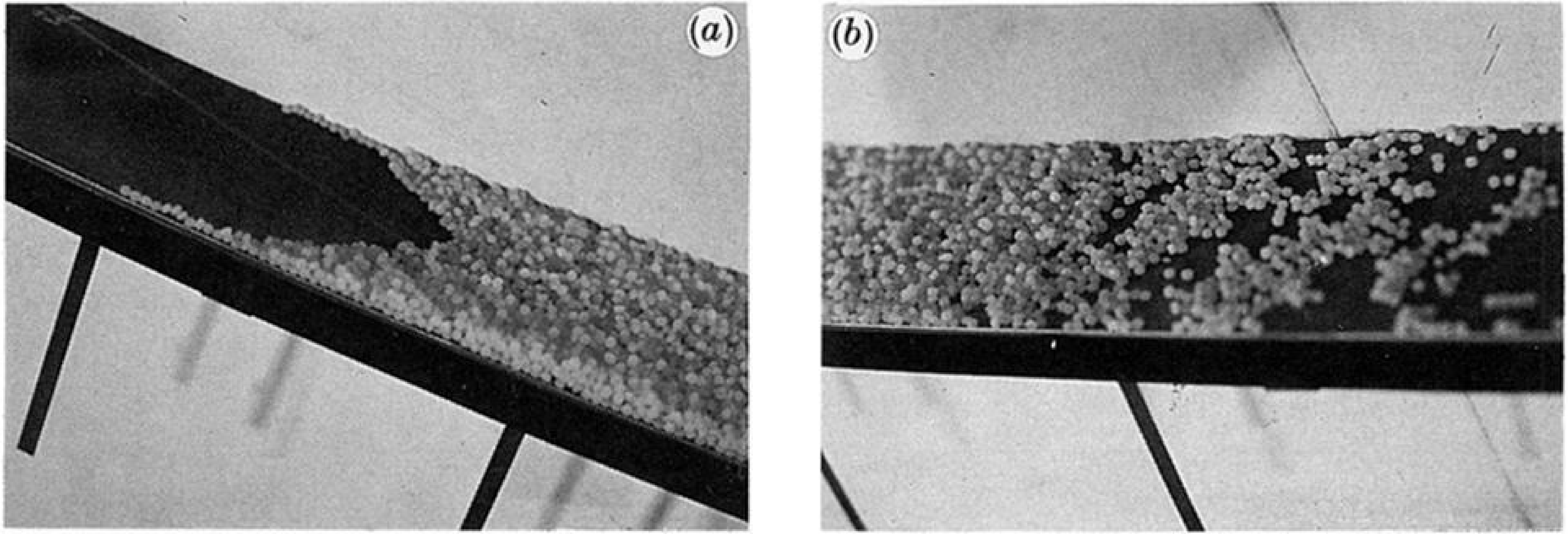

igure 10. (*a*) Photograph of the rear end of the granular avalanche (experiment 73) at rest, owing the parabolic-type distribution of the rear end across the width of the chute. (*b*) Leading ge of the settled granular avalanche for experiment 73, showing the large spread of the particles.